Geophysical Research Letters

Supporting Information for

Arctic rift system driven by a giant stagnant slab

Genti Toyokuni[1] and Dapeng Zhao[1]

1 Department of Geophysics, Graduate School of Science, Tohoku University, Sendai 980-8578, Japan

Contents of this file

- Figures S1 to S29
- Tables S1 and S2

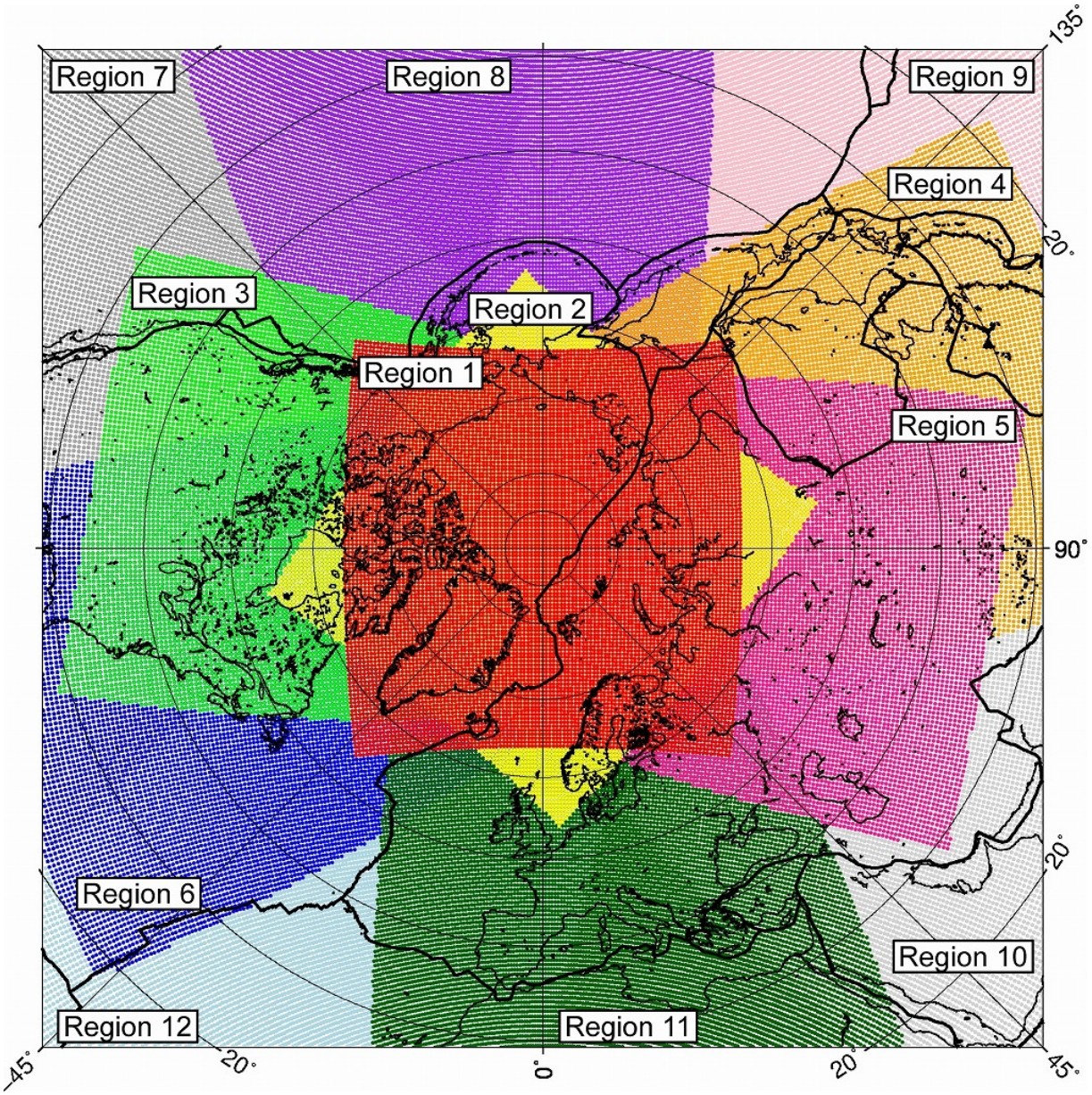

Figure S1. Distribution of Regions 1−12 listed in Table S1. The points denote the grid nodes adopted for interpolation to obtain the final tomographic model.

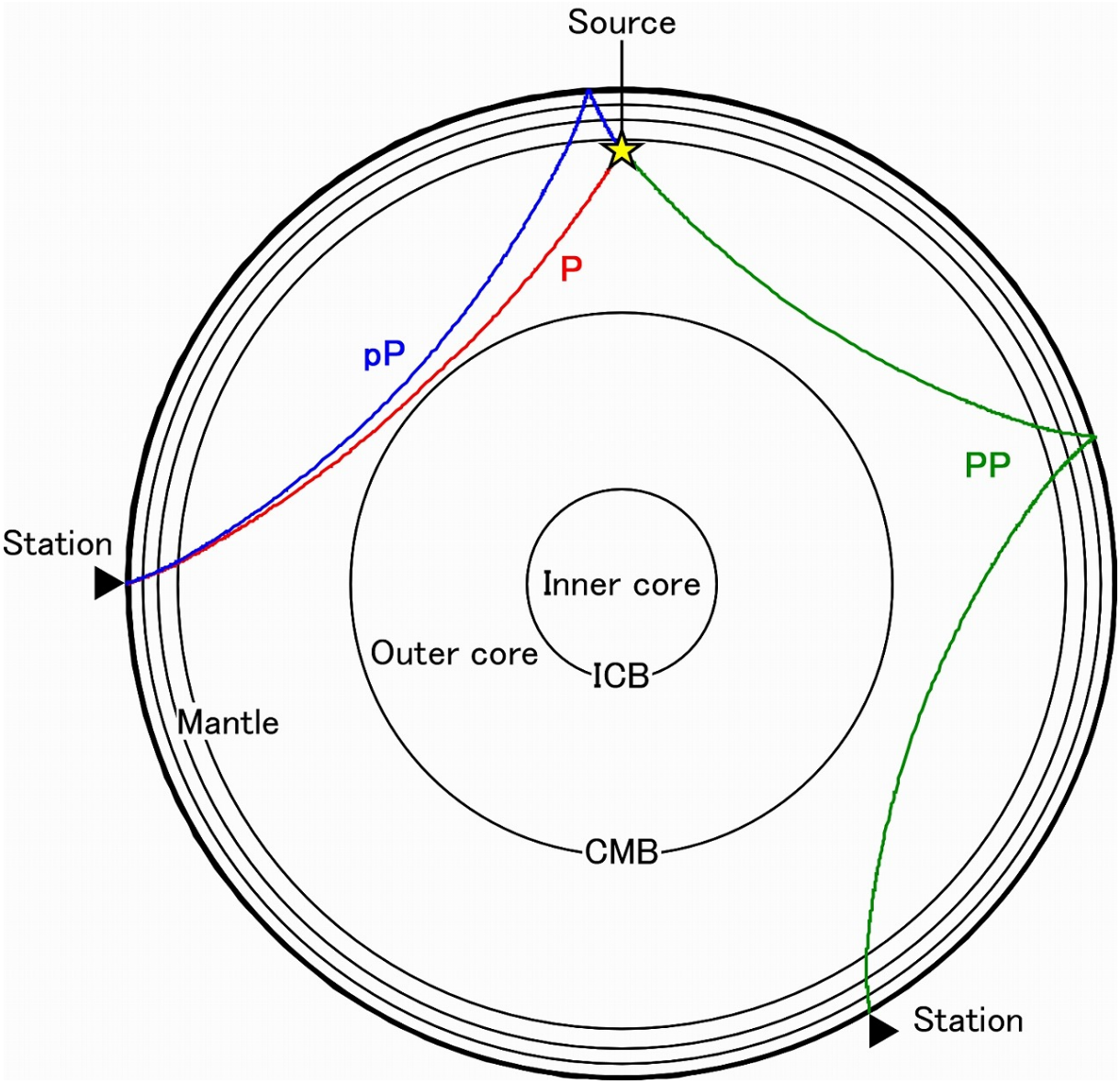

Figure S2. Schematic illustration of ray paths of *P*, *pP*, and *PP* waves. The yellow star denotes a hypocenter. The inverted triangles denote seismic stations.

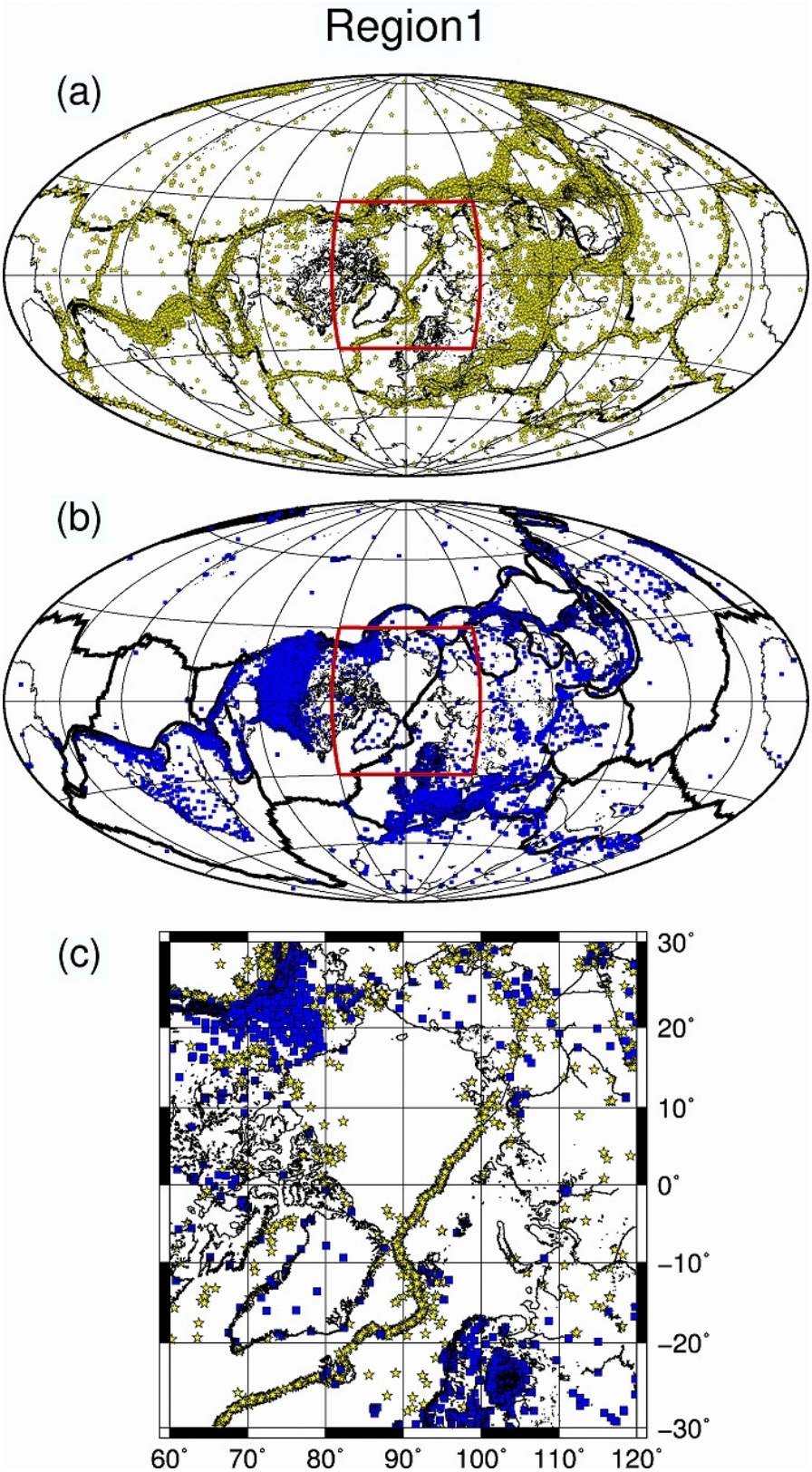

Figure S3.

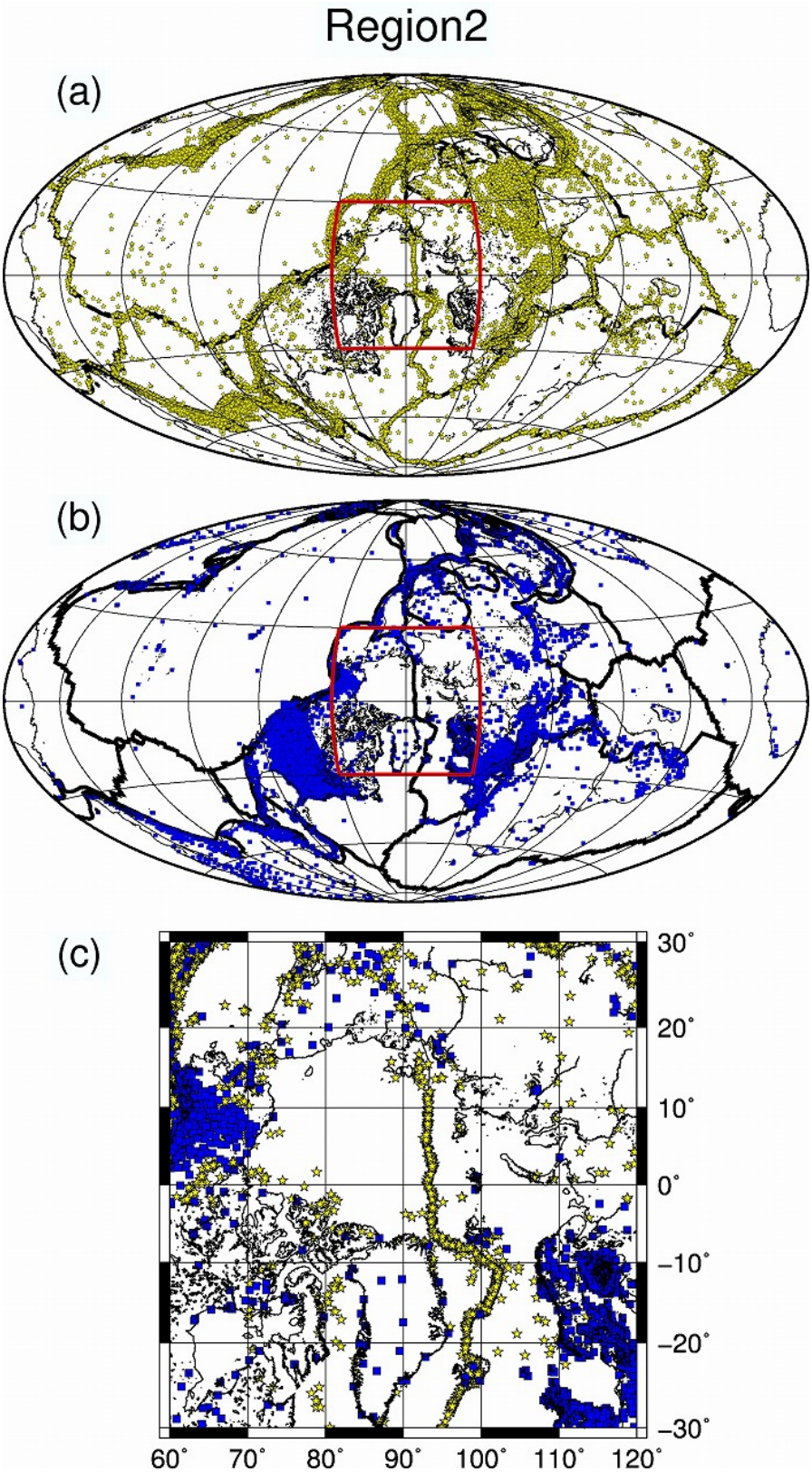

Figure S4.

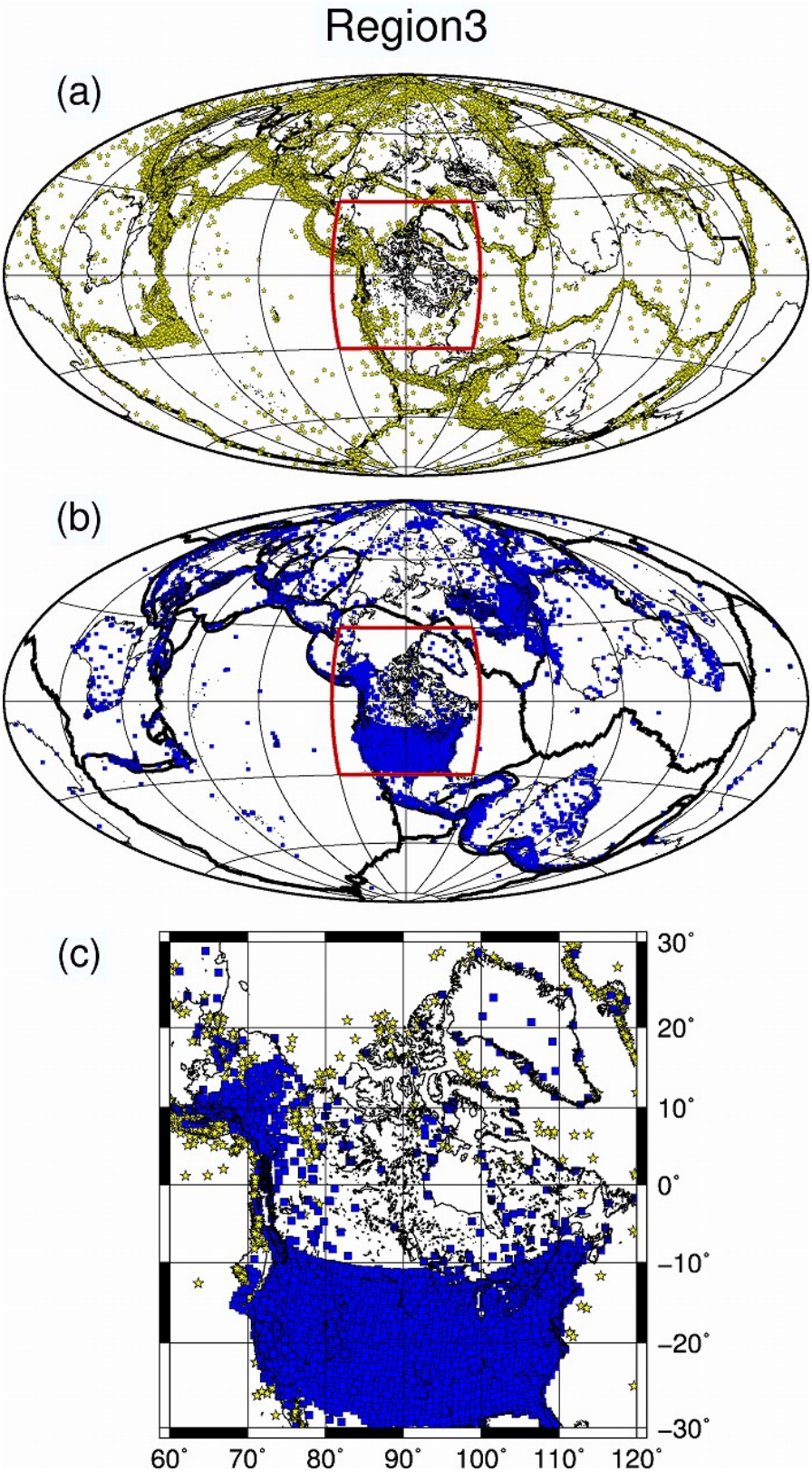

Figure S5.

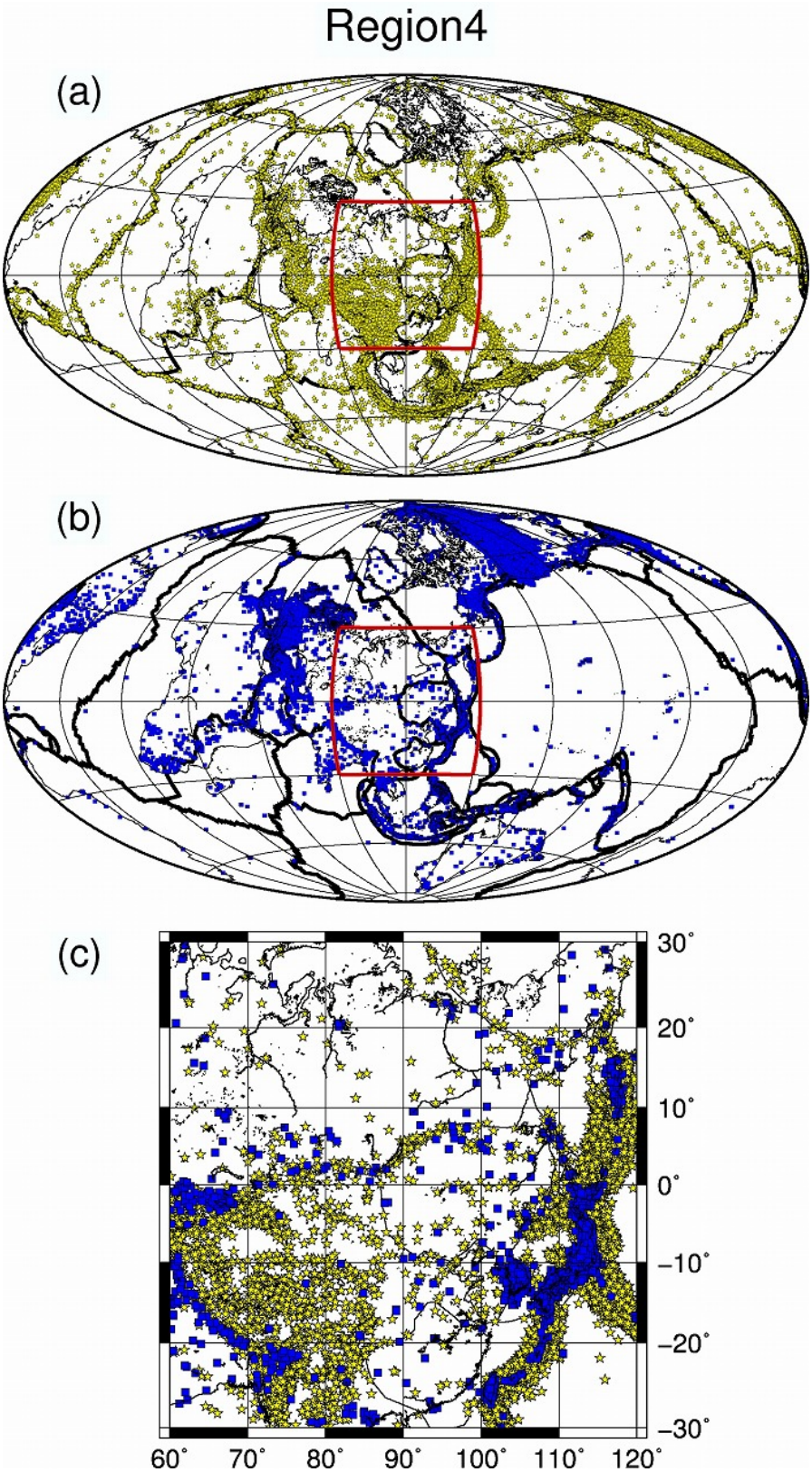

Figure S6.

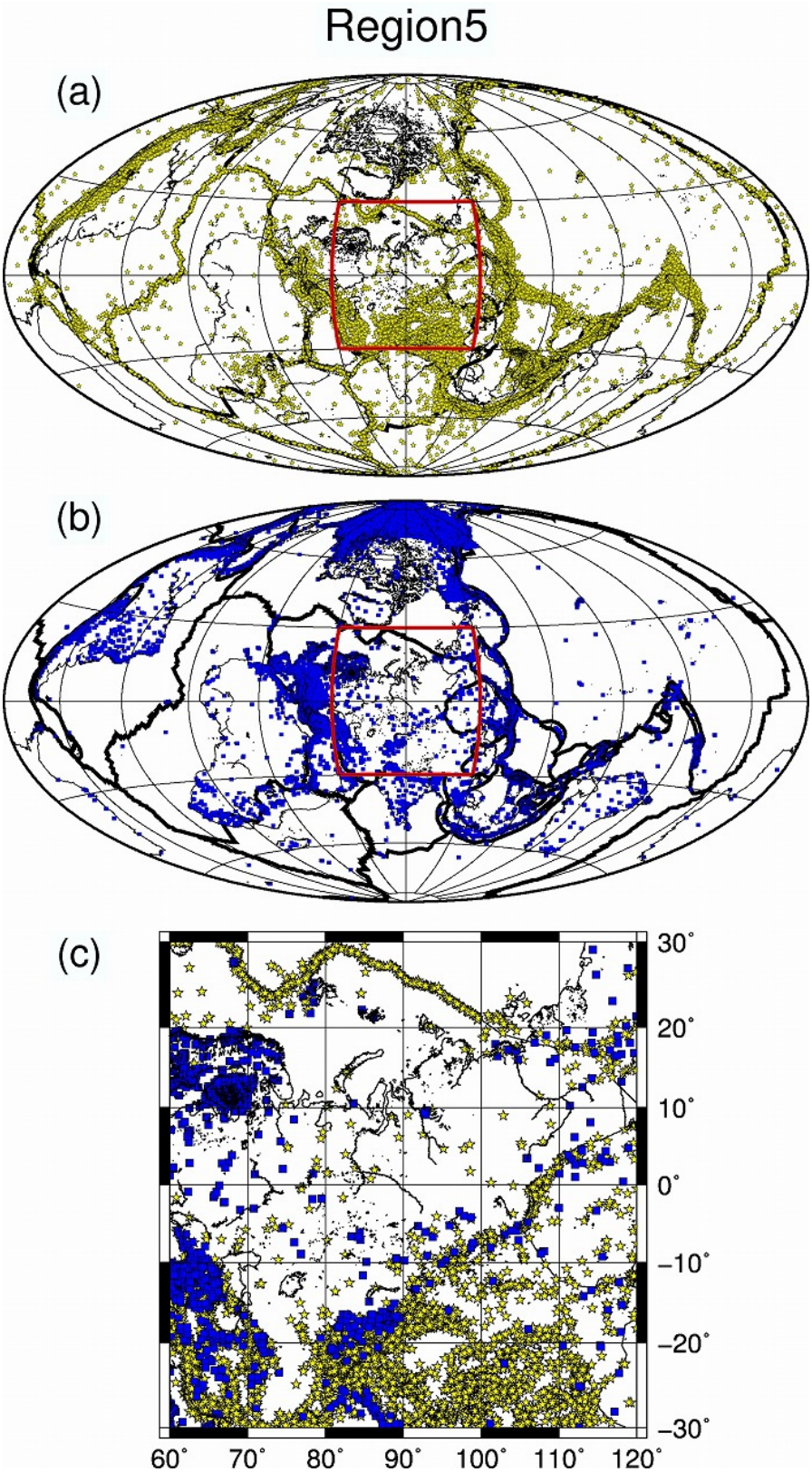

Figure S7.

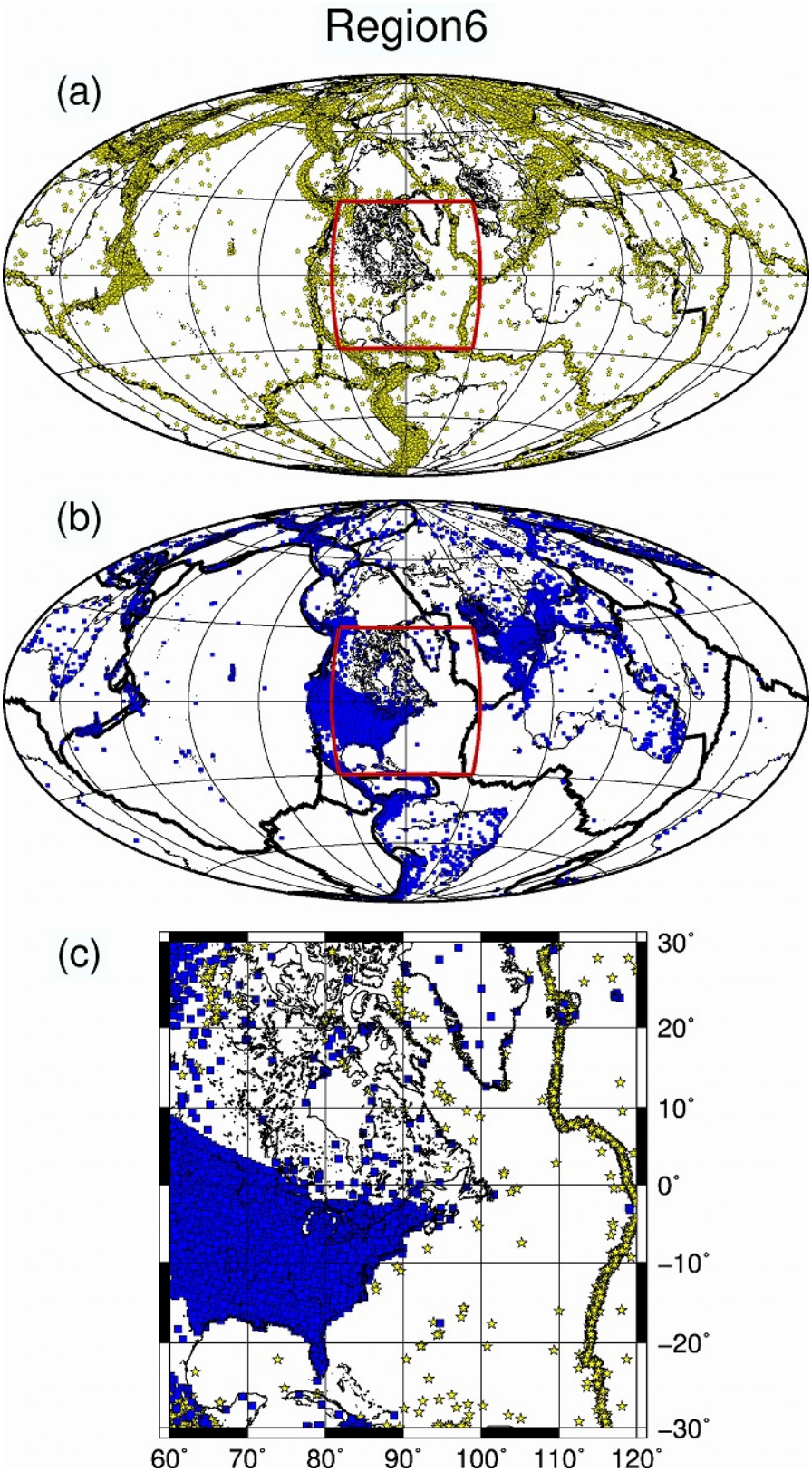

Figure S8.

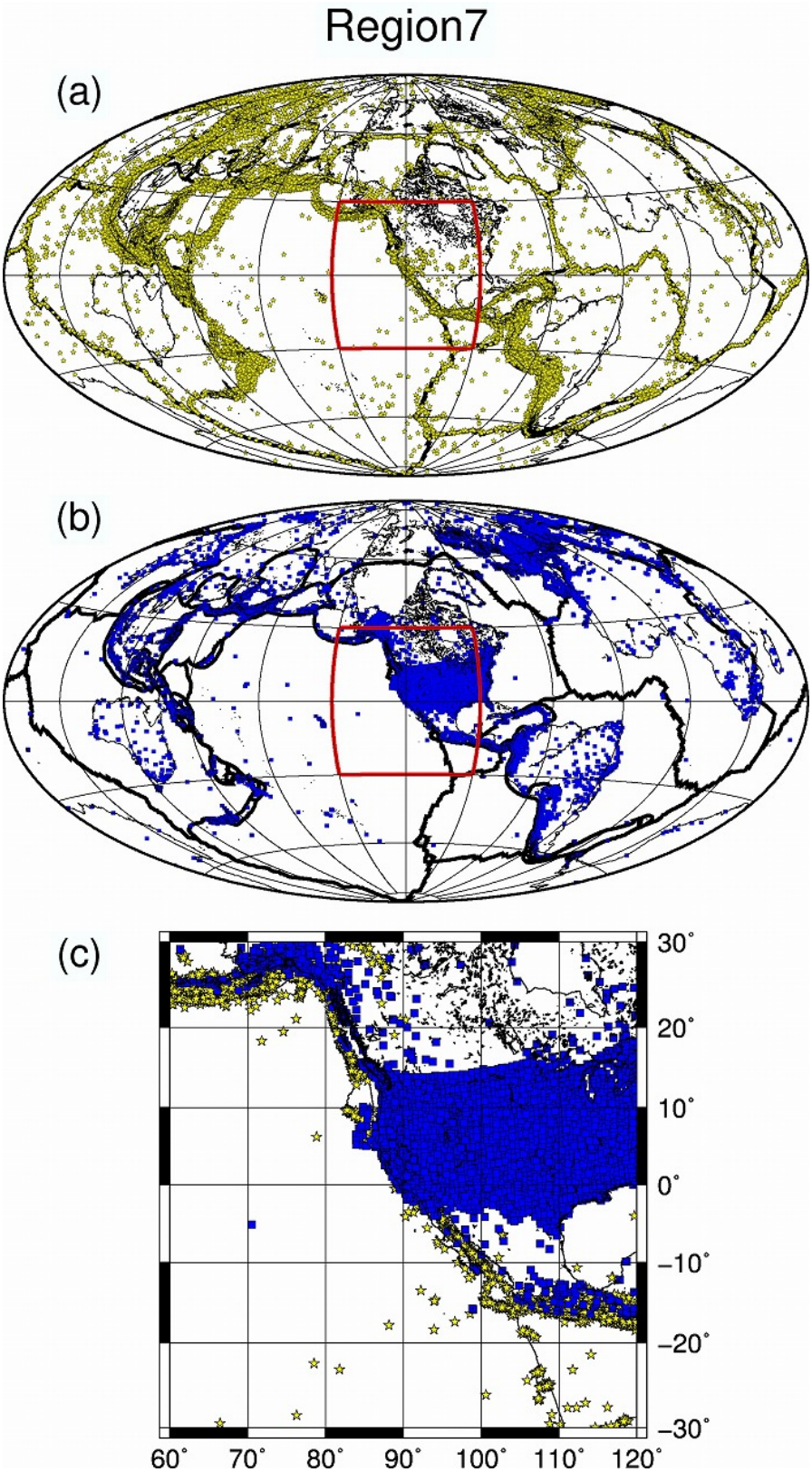

Figure S9.

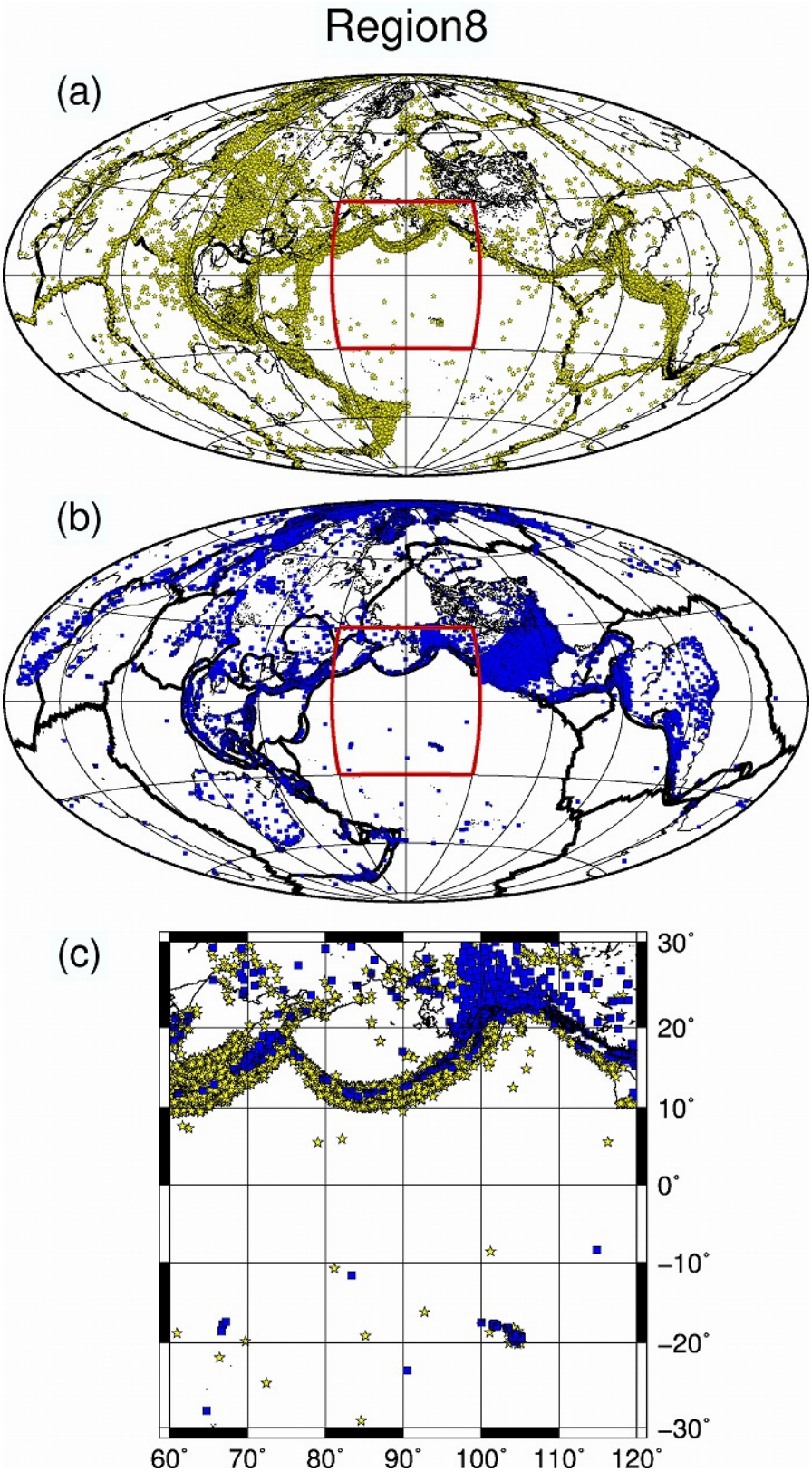

Figure S10.

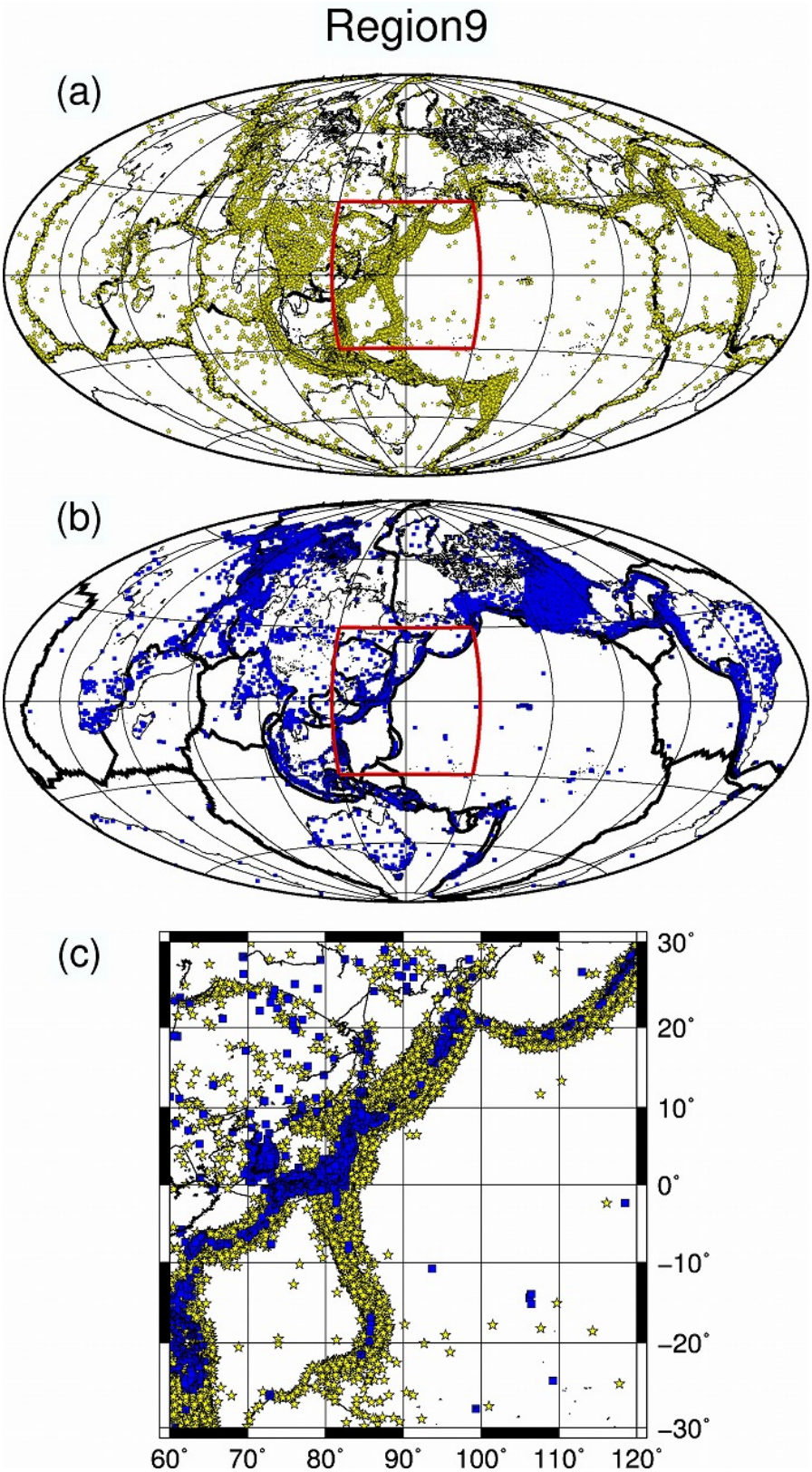

Figure S11.

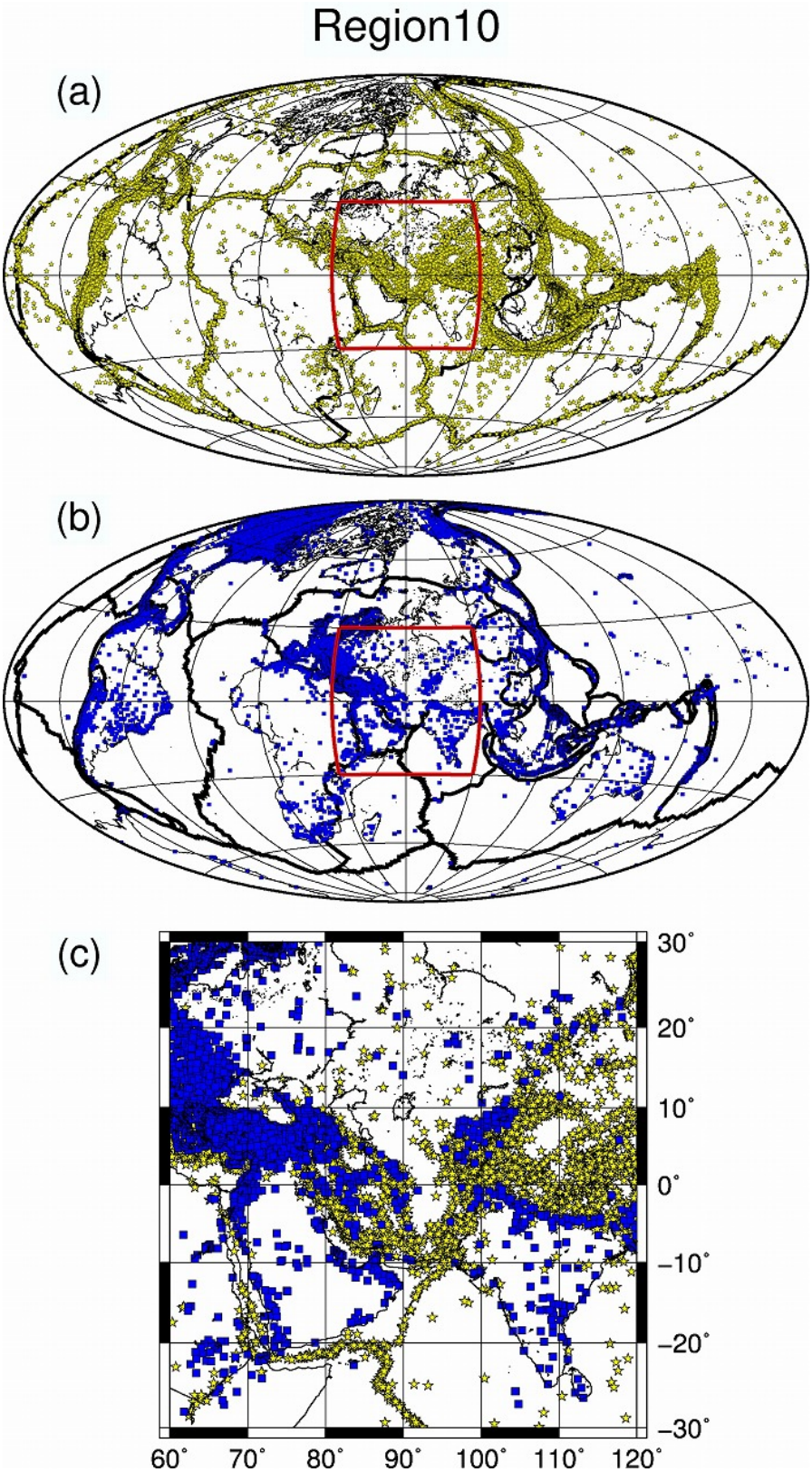

Figure S12.

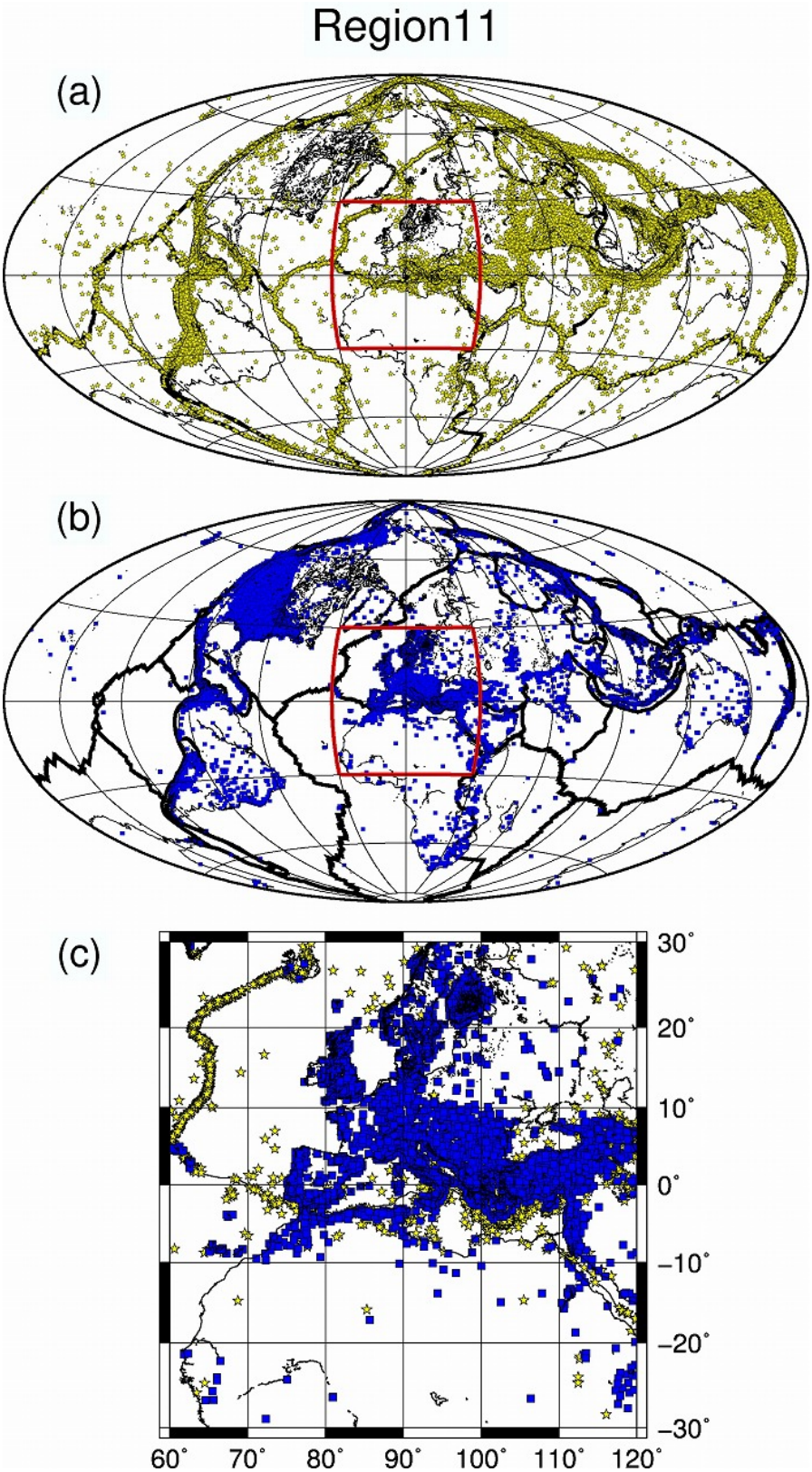

Figure S13.

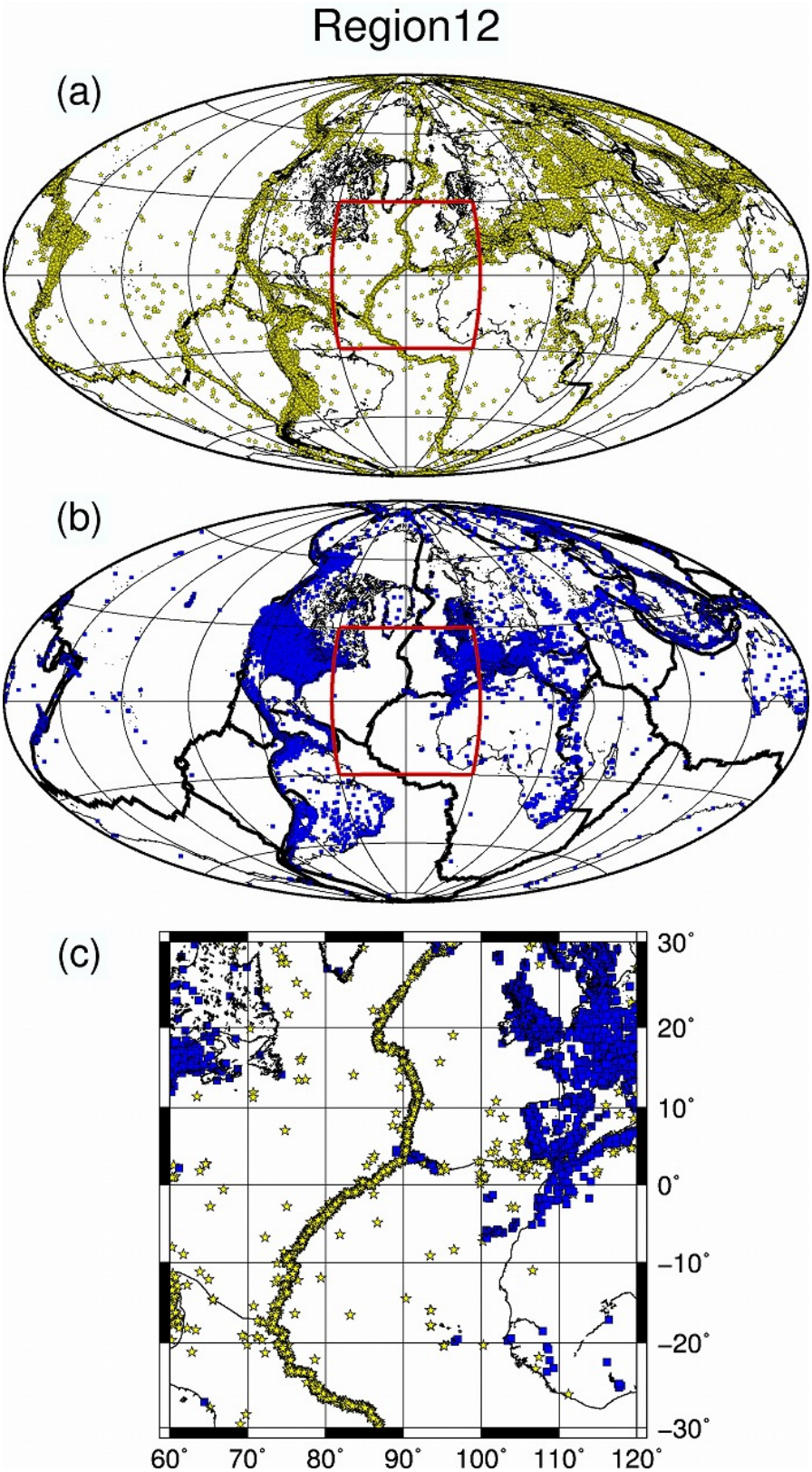

Figure S14.

Figure 3. Global distribution of **(a)** earthquakes and **(b)** seismic stations, and **(c)** distribution of seismic stations inside the target region, used in the tomographic inversion for Region 1. The thick black lines denote plate boundaries. The coordinate transformation is applied (see the text for details).

Figure 4. The same as Figure 3 but for Region 2.

Figure 5. The same as Figure 3 but for Region 3.

Figure 6. The same as Figure 3 but for Region 4.

Figure 7. The same as Figure 3 but for Region 5.

Figure 8. The same as Figure 3 but for Region 6.

Figure 9. The same as Figure 3 but for Region 7.

Figure 10. The same as Figure 3 but for Region 8.

Figure 11. The same as Figure 3 but for Region 9.

Figure 12. The same as Figure 3 but for Region 10.

Figure 13. The same as Figure 3 but for Region 11.

Figure 14. The same as Figure 3 but for Region 12.

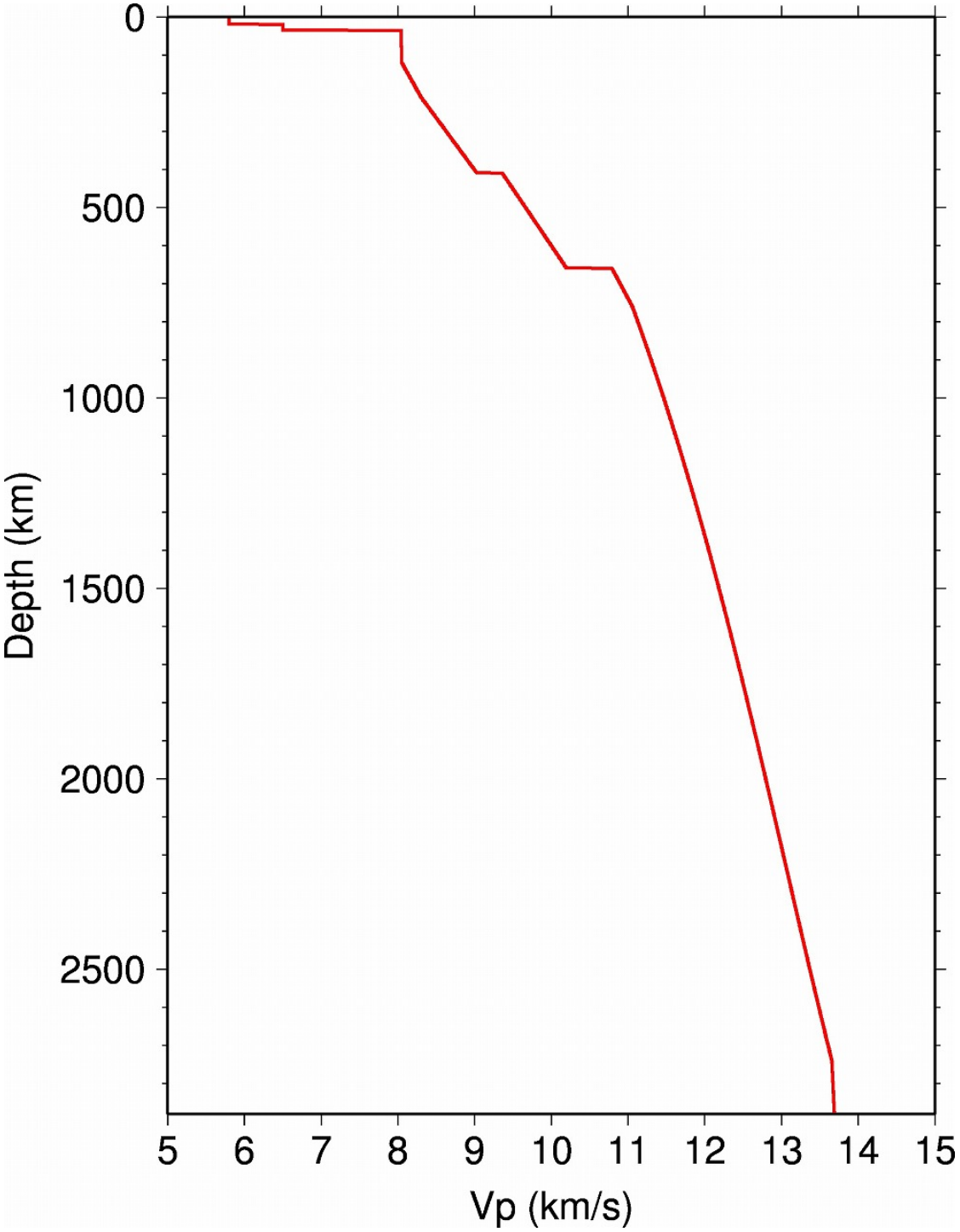

Figure S15. The starting 1-D *P* wave velocity model (IASP91) (Kennett & Engdahl, 1991) adopted for 3-D tomographic inversions.

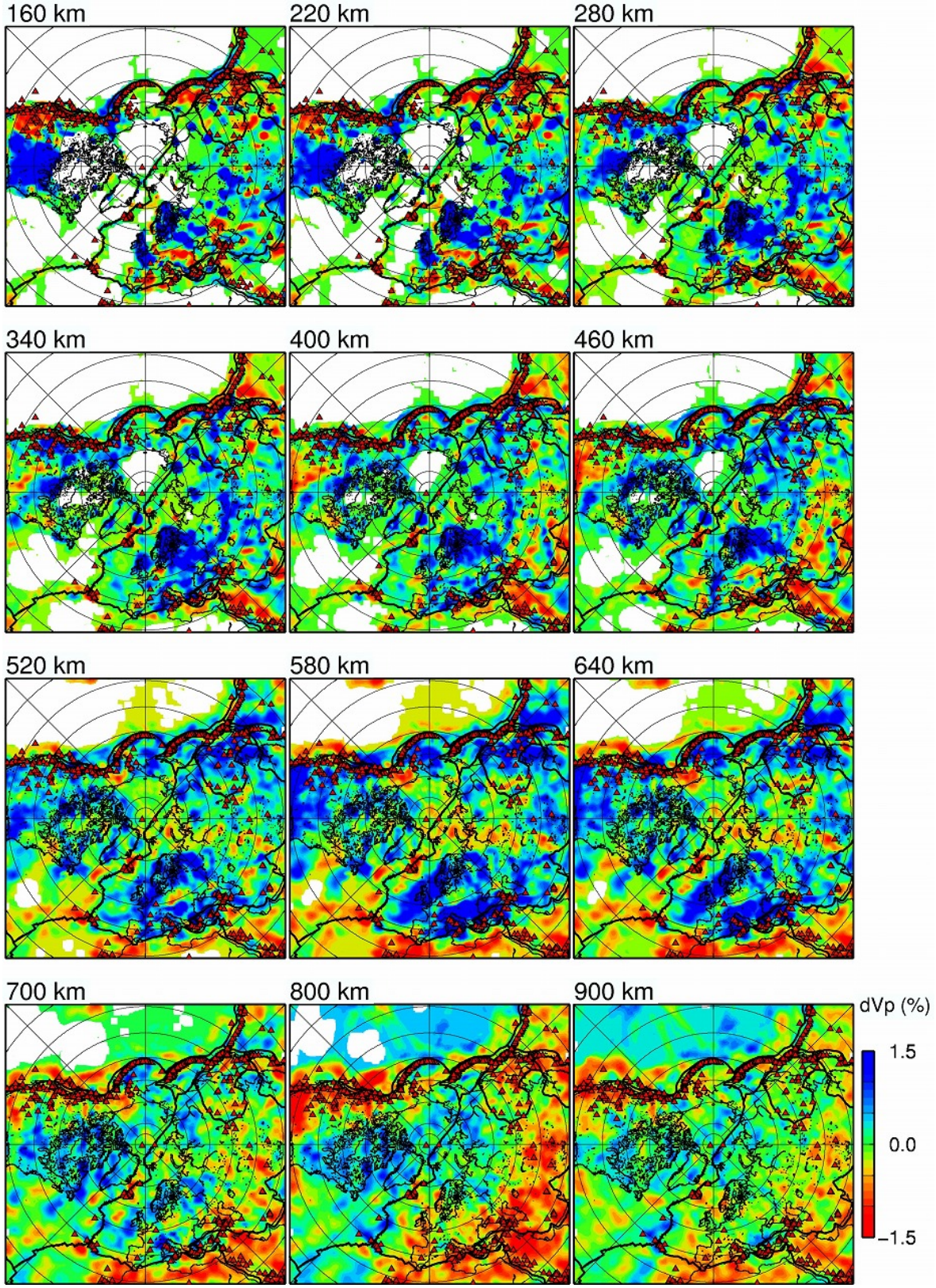
160 km
220 km
280 km
340 km
400 km
460 km
520 km
580 km
640 km
700 km
800 km
900 km
dVp (%)
1.5
0.0
−1.5

Figure S16.

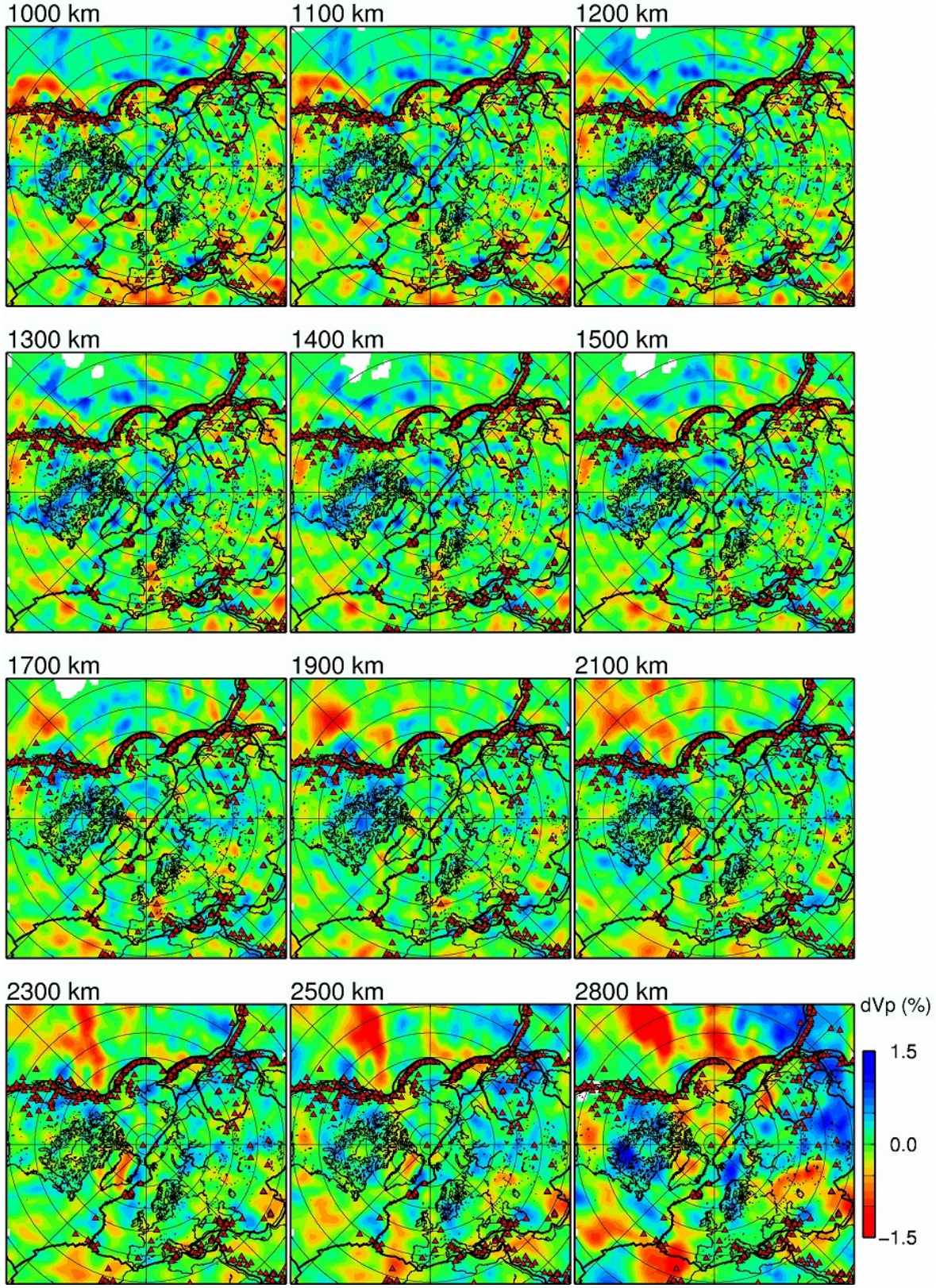

Figure S16. (continued)

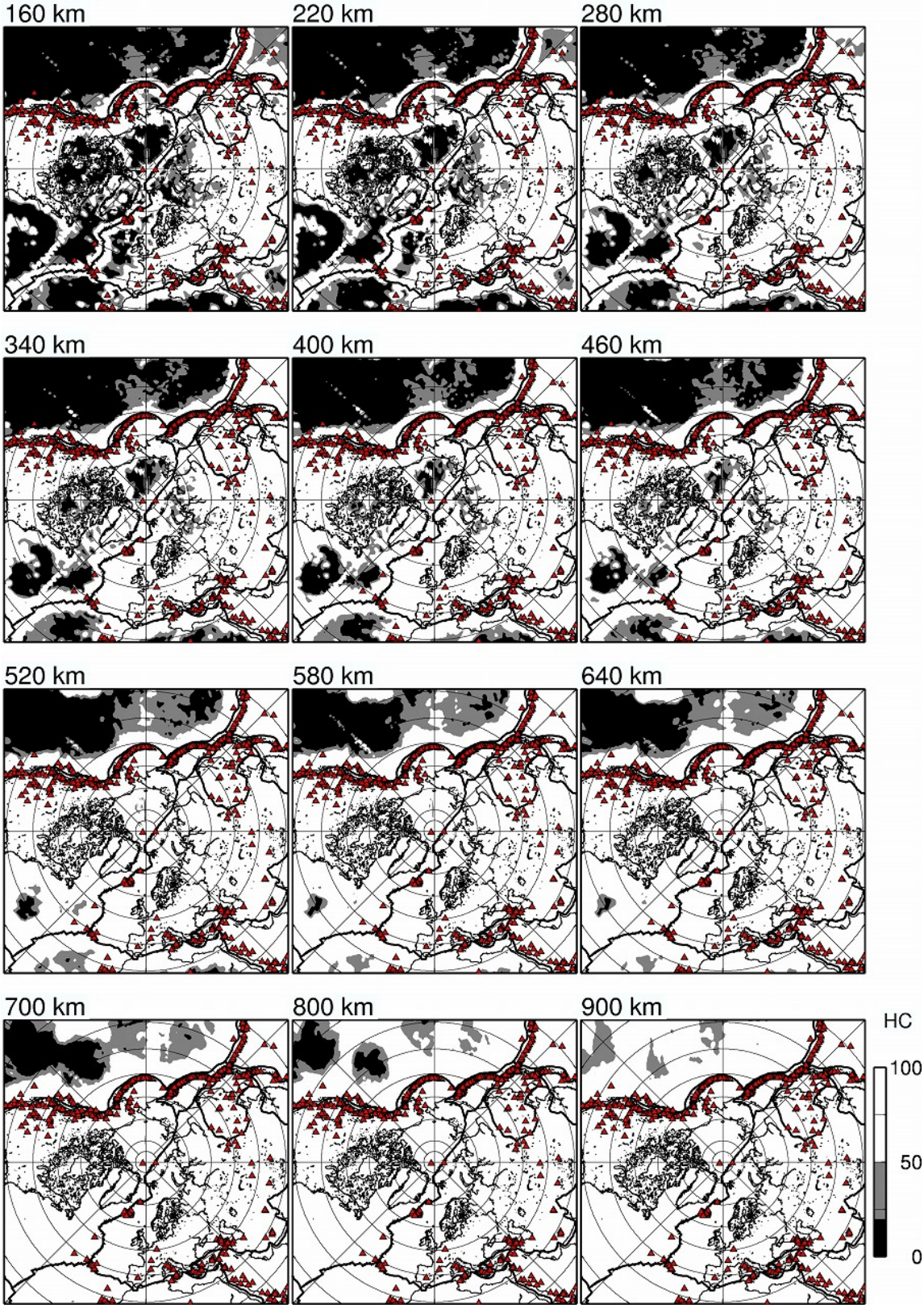
160 km
220 km
280 km
340 km
400 km
460 km
520 km
580 km
640 km
700 km
800 km
900 km
HC
100
50
0

Figure S17.

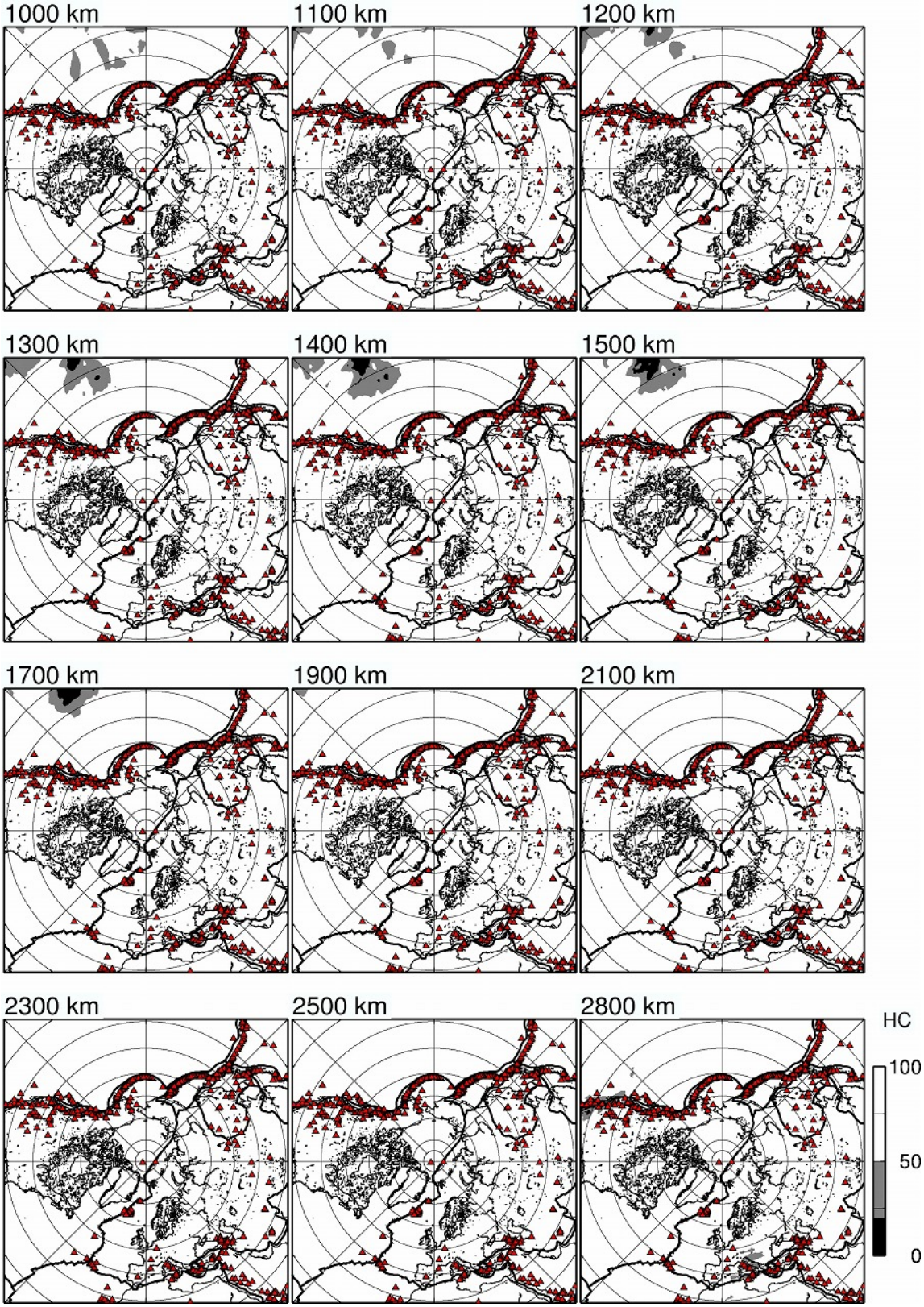

Figure S17. (continued)

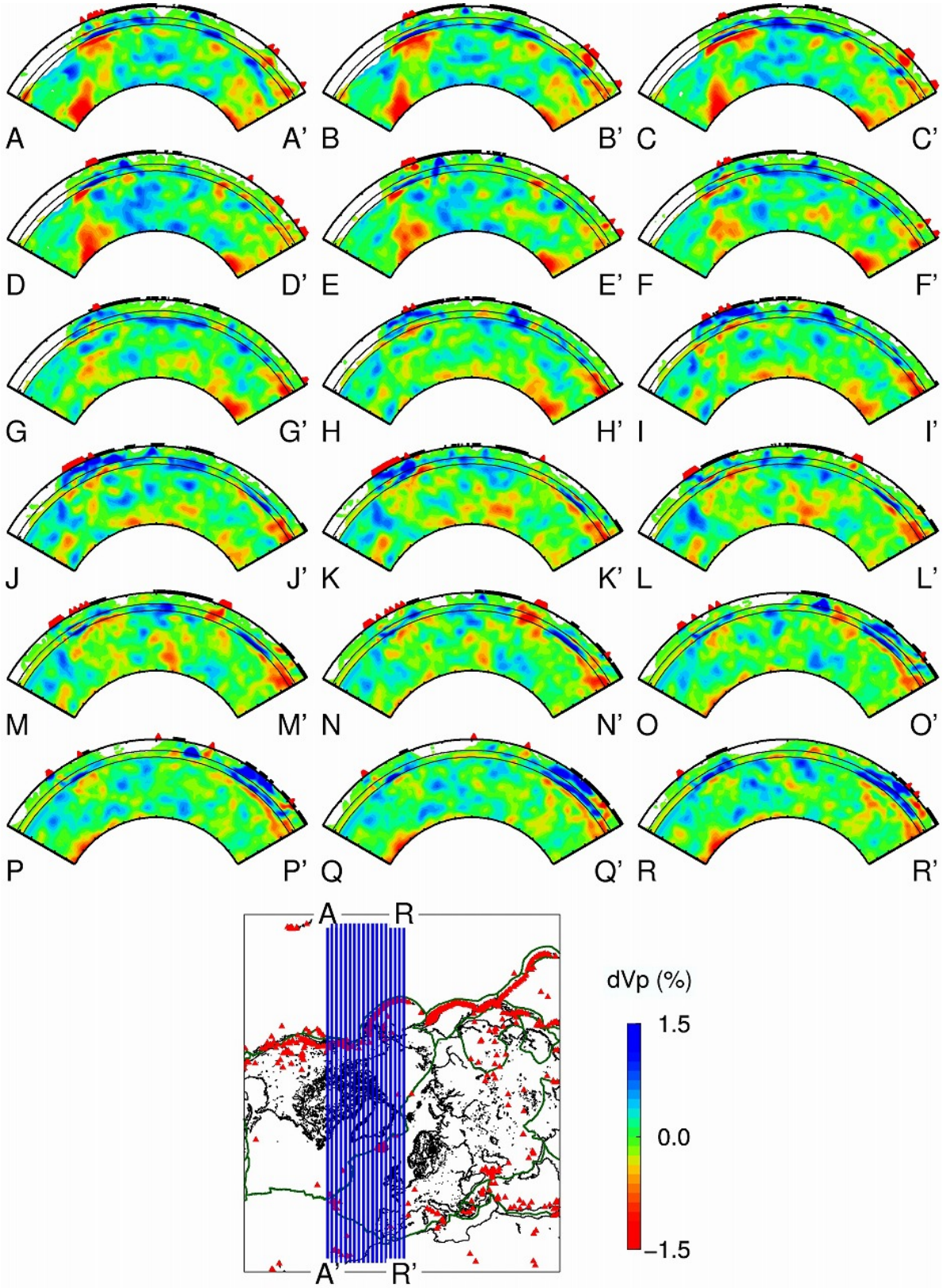

Figure S18.

Figure S16. Map views of Vp tomography. The layer depth is shown above each map. The blue and red colors denote high and low Vp perturbations, respectively, whose scale (in %) is shown on the right. Areas with average hit counts < 20 are masked in white. Red triangles: active volcanoes; thick black lines: plate boundaries.

Figure S17. Map views of average ray hit count (HC). The layer depth is shown above each map. The HC scale is shown on the right. The areas in black color with hit HC < 20 are masked in the resulting tomographic images. Red triangles: active volcanoes; thick black lines: plate boundaries.

Figure S18. Vertical cross sections of Vp tomography along 18 profiles beneath North America and Greenland as shown on the inset map. The 410-km and 660-km discontinuities are shown in black solid lines. The thick black lines on the surface denote land areas. Active volcanoes within a ±2° width of each profile are shown as red triangles. Other labels are the same as those in Figure 3.

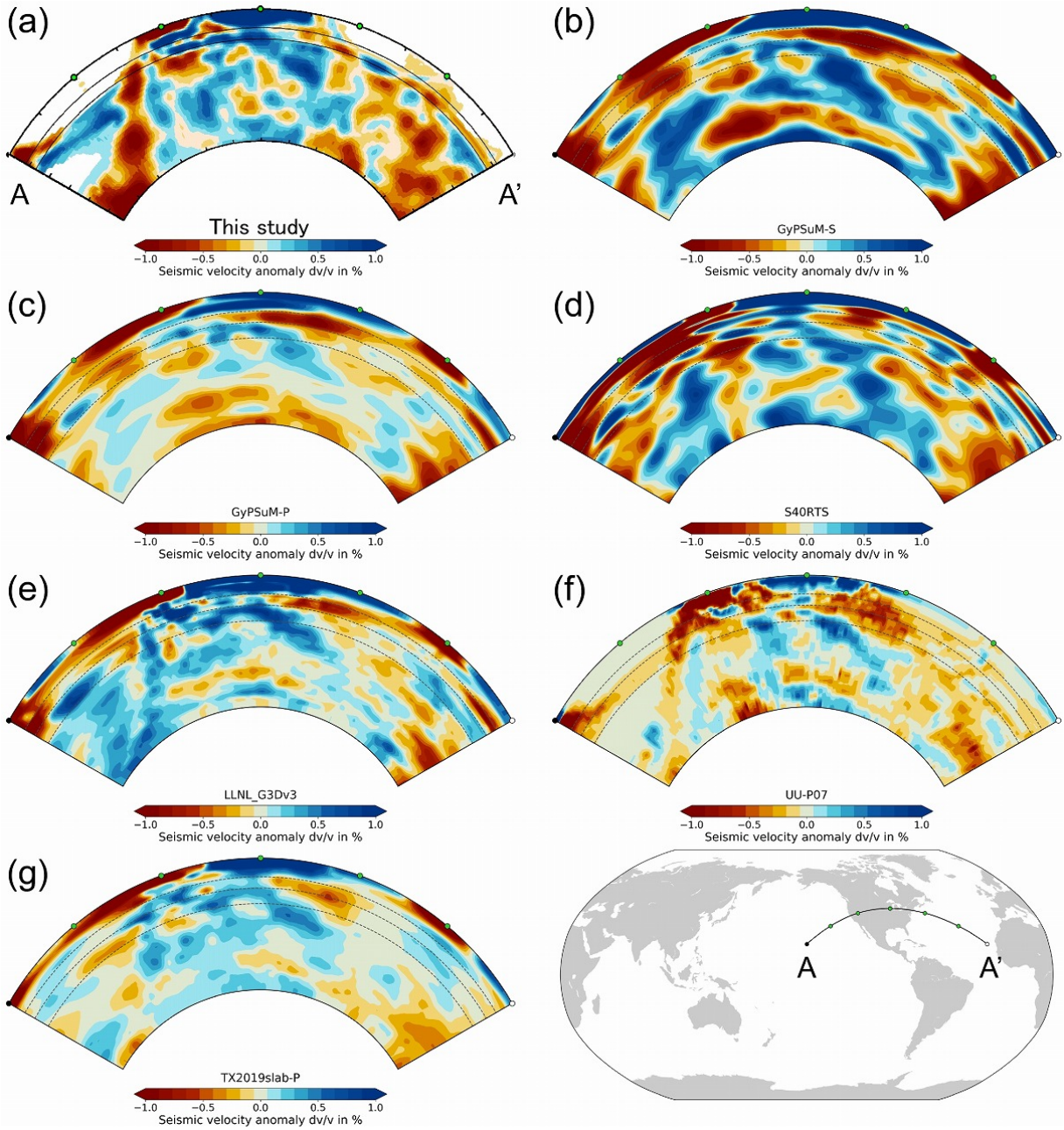

Figure S19. Comparison of tomographic models along A-A' profile on the inset map. **(a)** This study, **(b)** GyPSuM-S (Simmons et al., 2010), **(c)** GyPSuM-P (Simmons et al., 2010), **(d)** S40RTS (Ritsema et al., 2011), **(e)** LLNL_G3Dv3 (Simmons et al., 2012), **(f)** UU-P07 (Amaru, 2007), and **(g)** TX2019slab-P (Lu et al., 2019). The same color scale is adopted for all models. The cross sections **(b)−(g)** are generated at the SubMachine site (https://www.earth.ox.ac.uk/~smachine/cgi/index.php) (Hosseini et al., 2018).

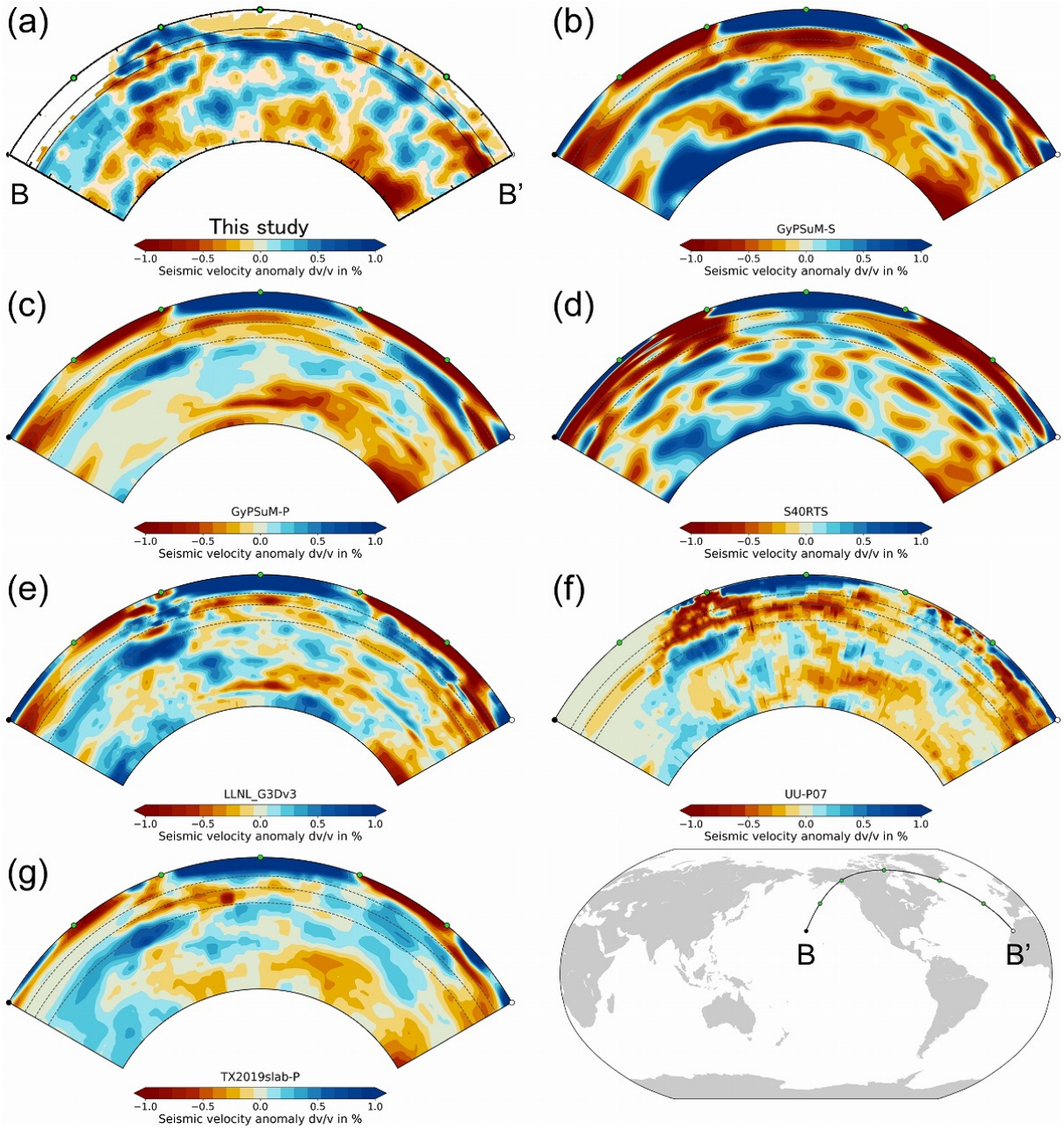

Figure S20. The same as Figure S19 but along B-B' profile on the inset map.

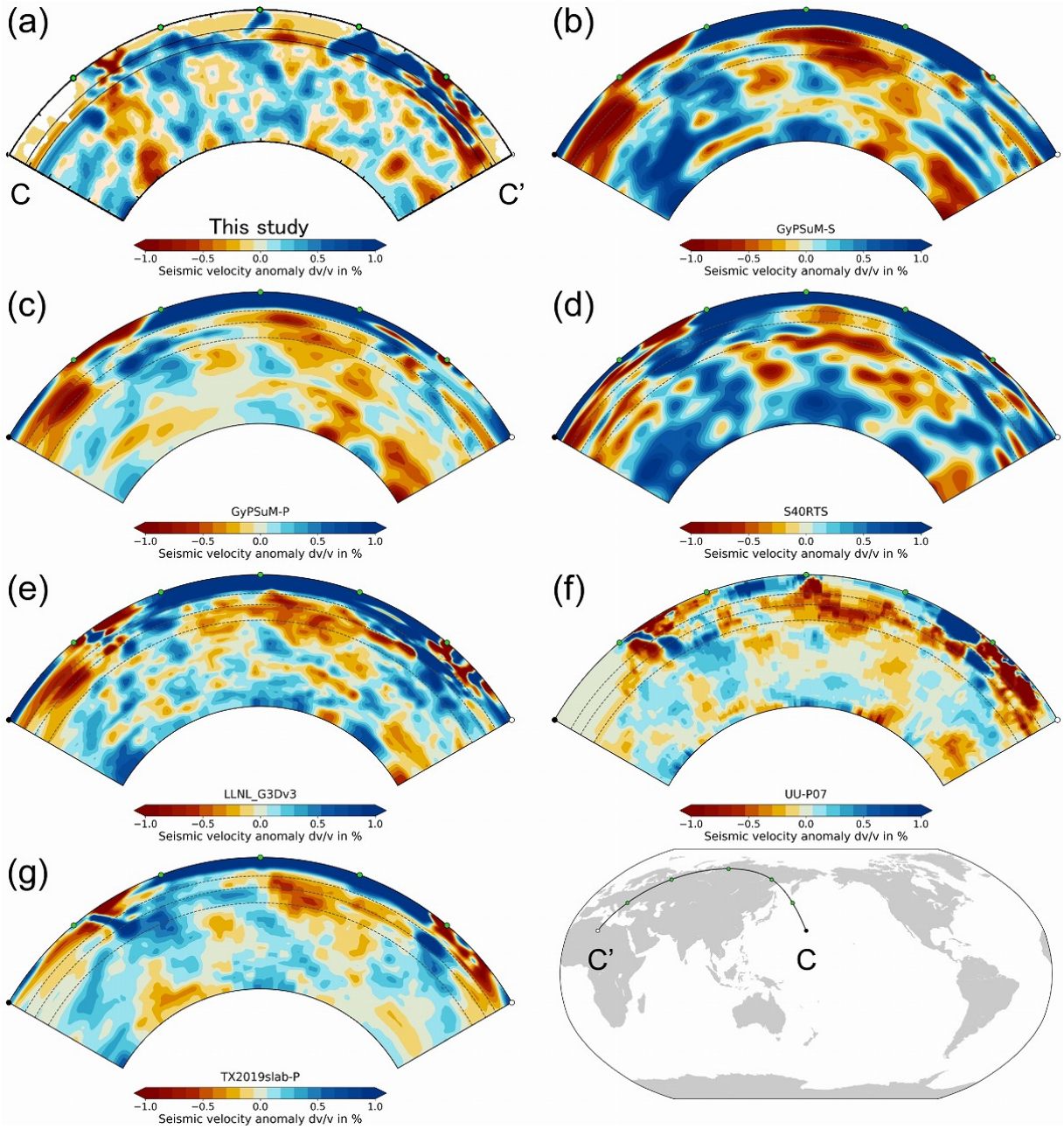

Figure S21. The same as Figure S19 but along B-B' profile on the inset map.

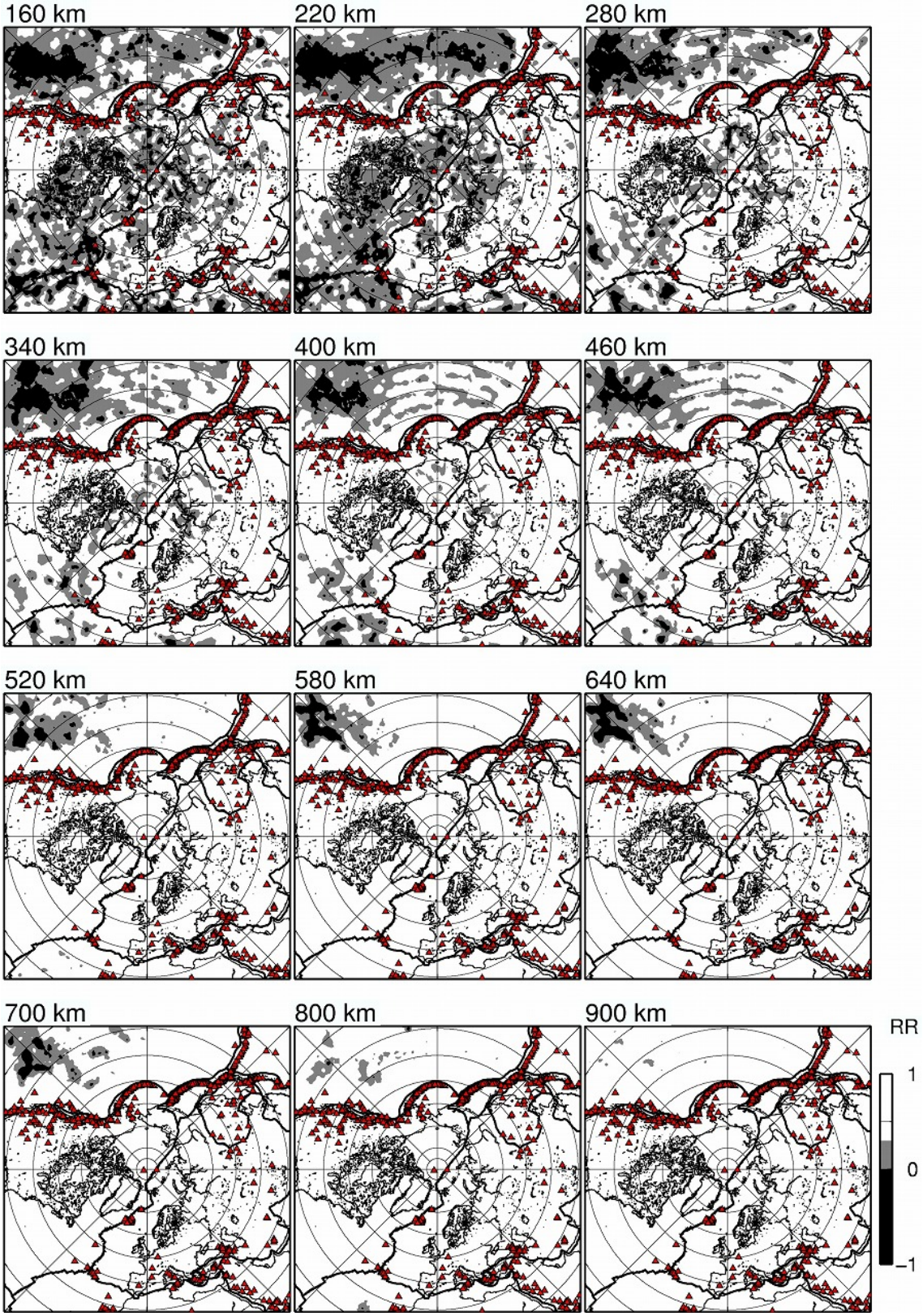
160 km
220 km
280 km
340 km
400 km
460 km
520 km
580 km
640 km
700 km
800 km
900 km
RR
1
0
−1

Figure S22.

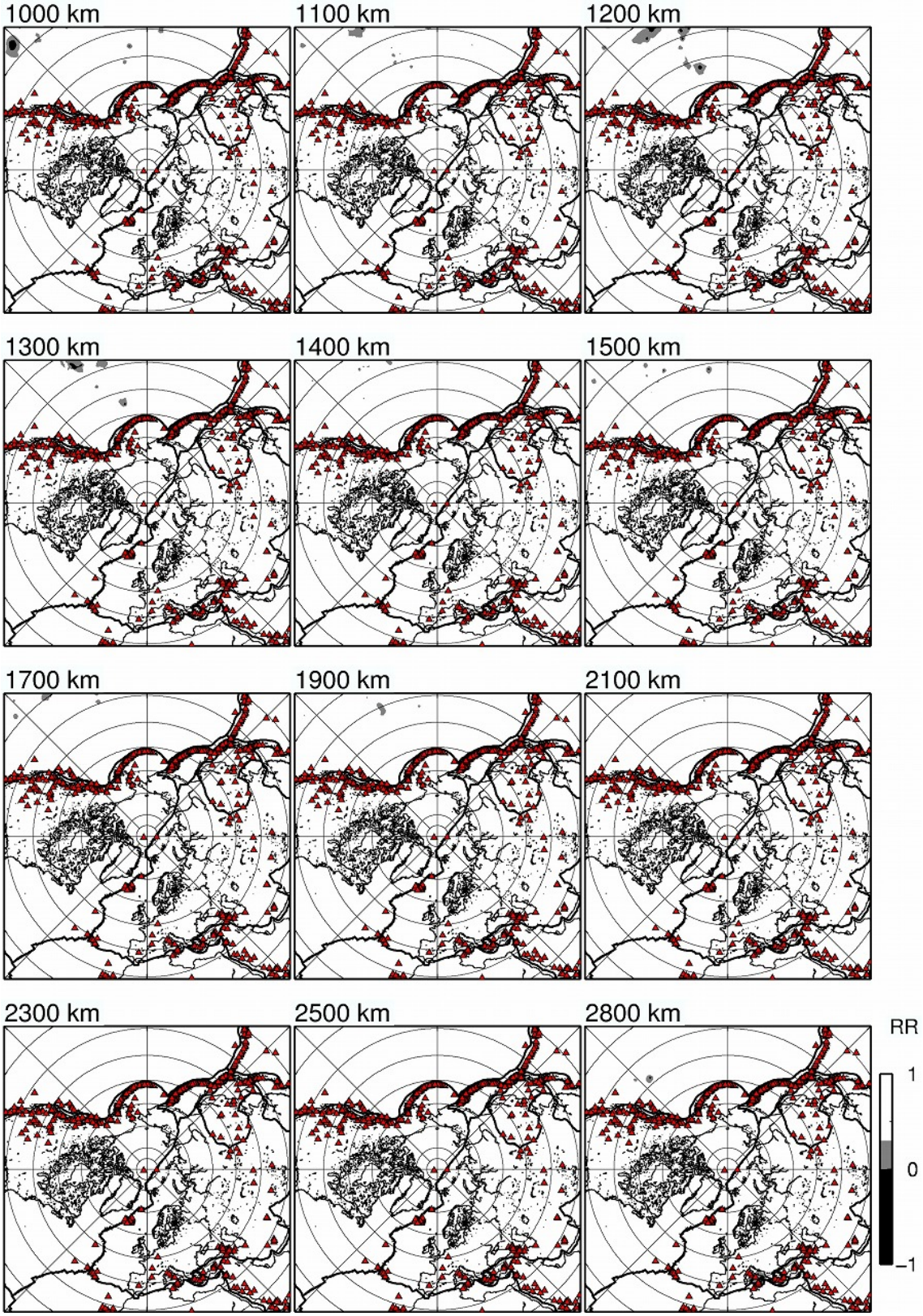

Figure S22. (continued)

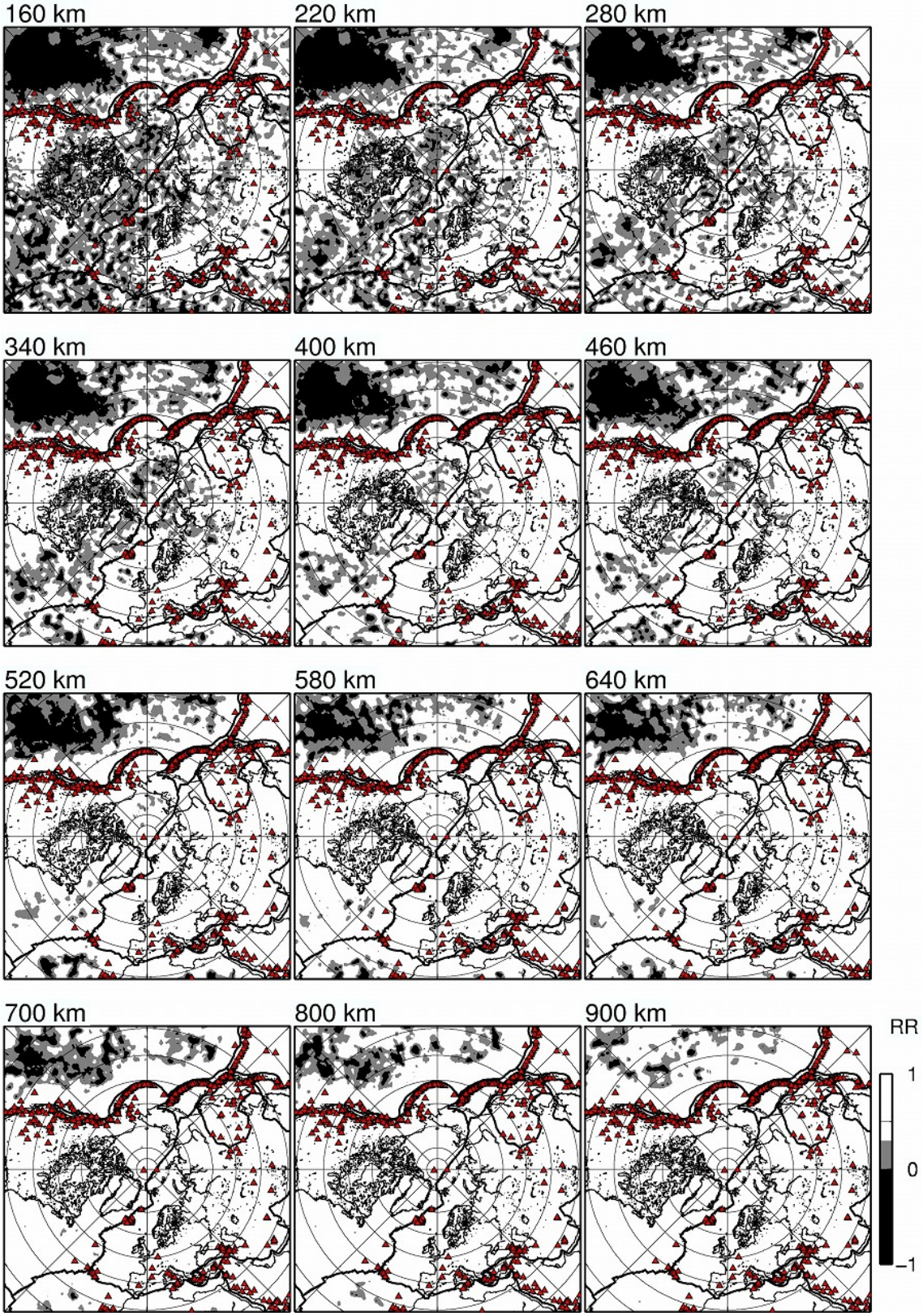
160 km
220 km
280 km
340 km
400 km
460 km
520 km
580 km
640 km
700 km
800 km
900 km
RR
1
0
−1

Figure S23.

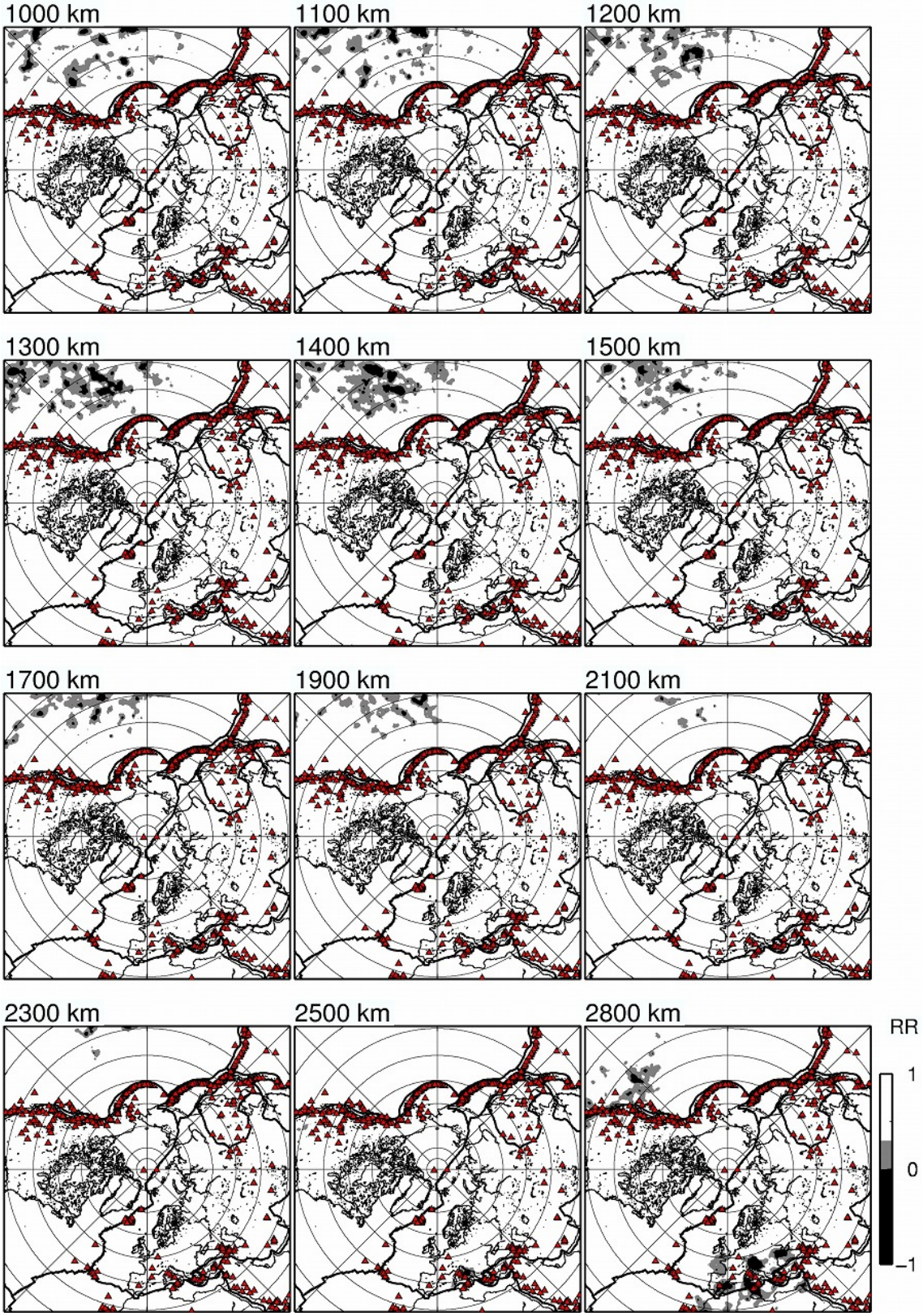

Figure S23. (continued)

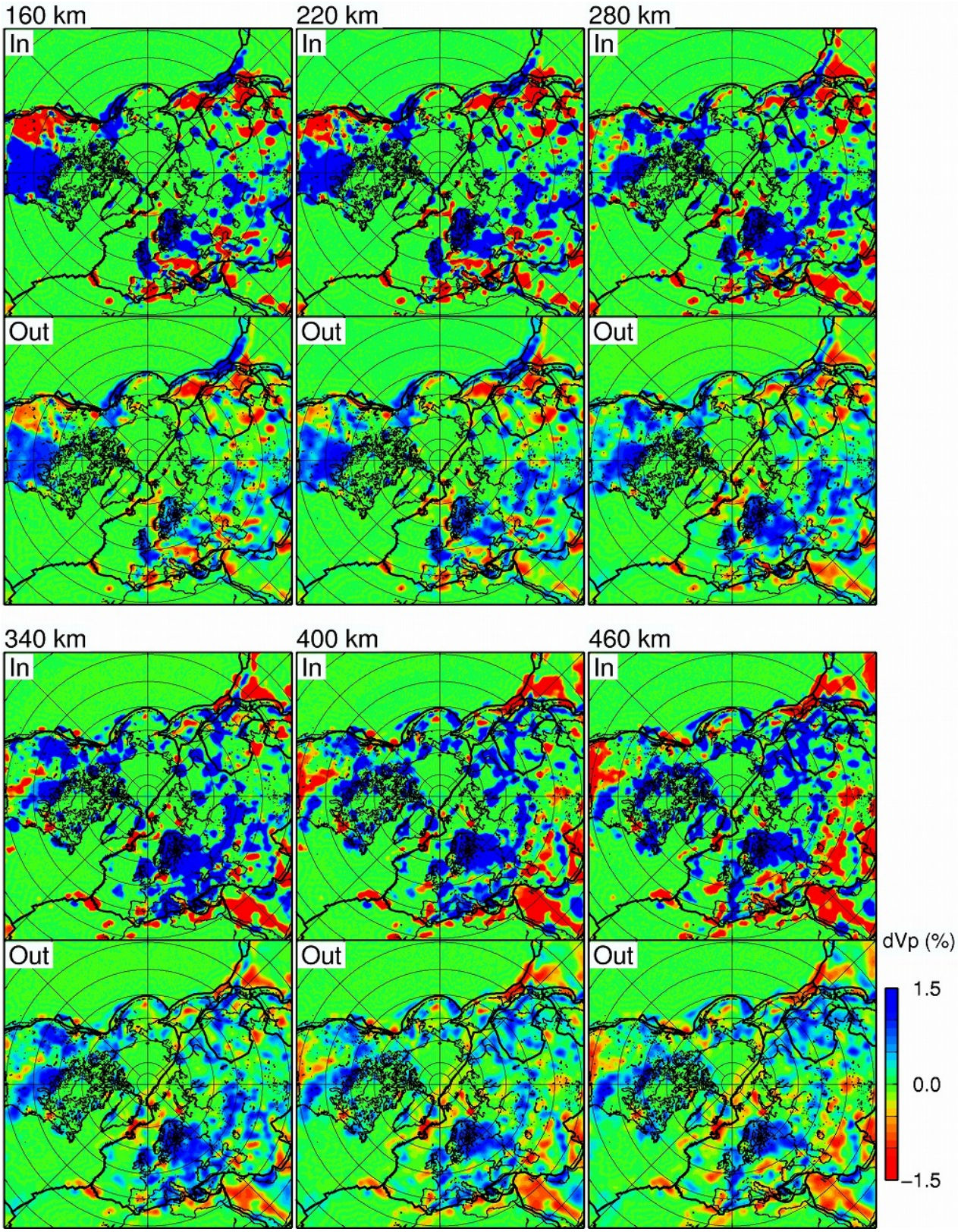
160 km
In
Out
220 km
In
Out
280 km
In
Out
340 km
In
Out
400 km
In
Out
460 km
In
Out
dVp (%)
1.5
0.0
−1.5

Figure S24.

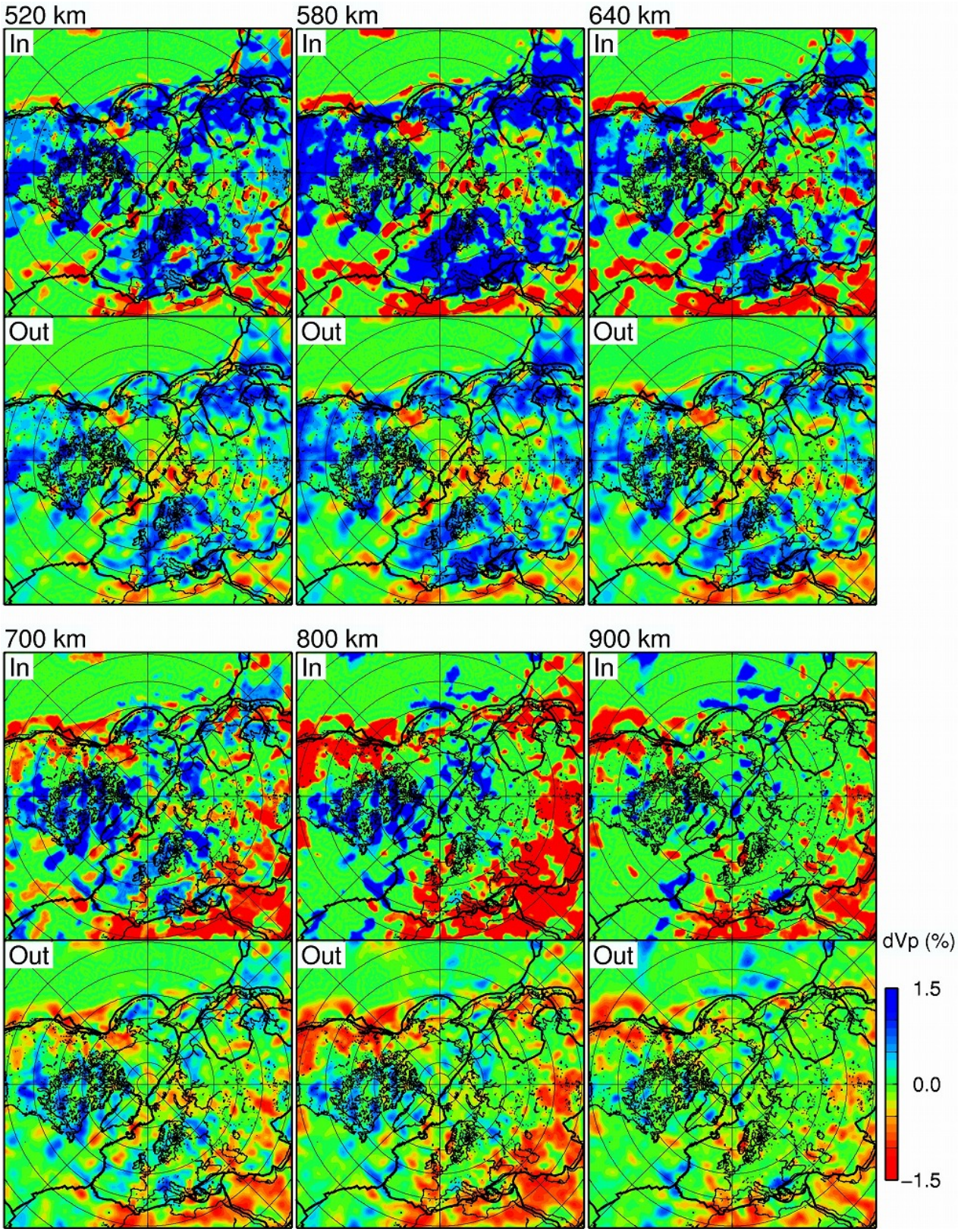

Figure S24. (continued)

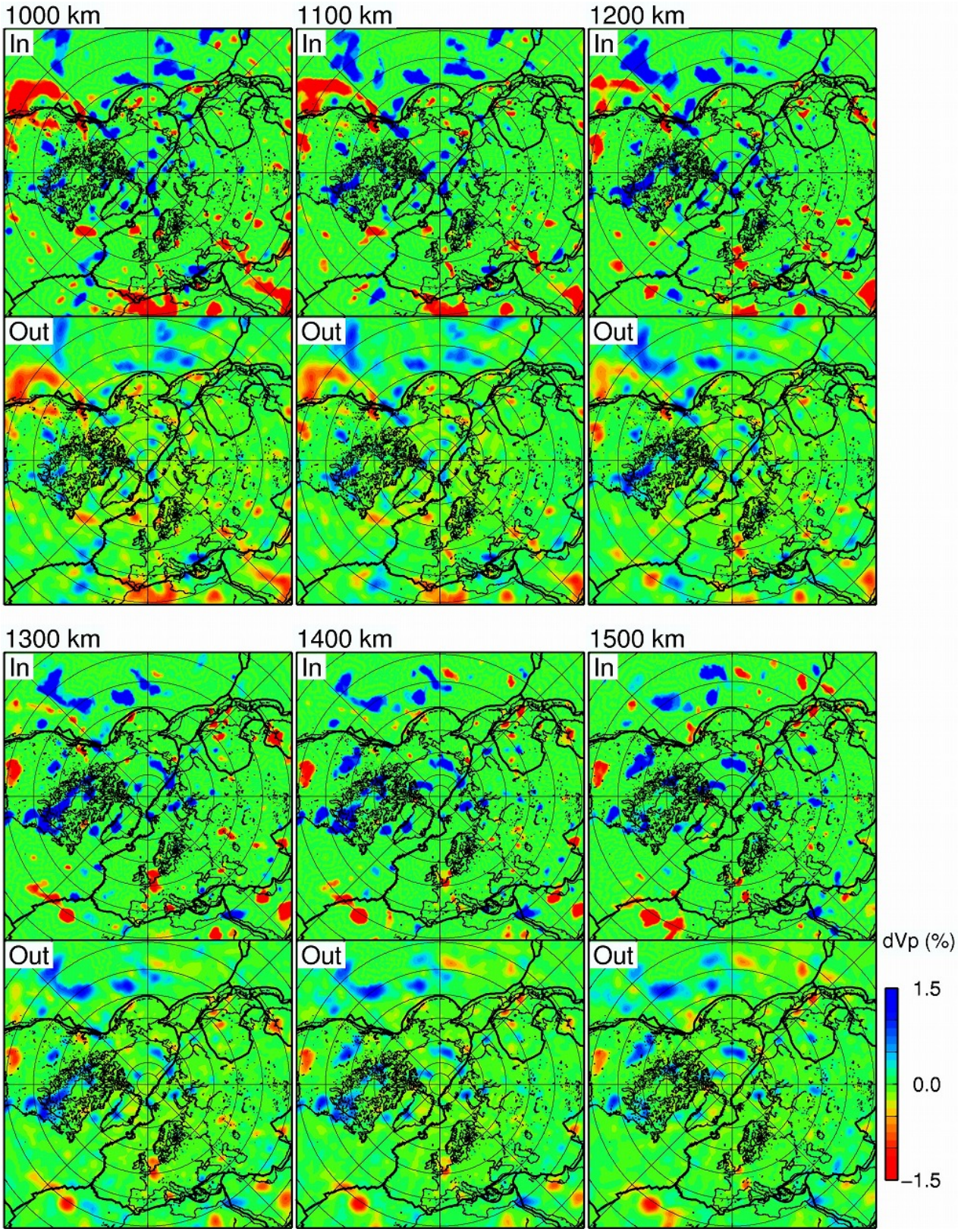

Figure S24. (continued)

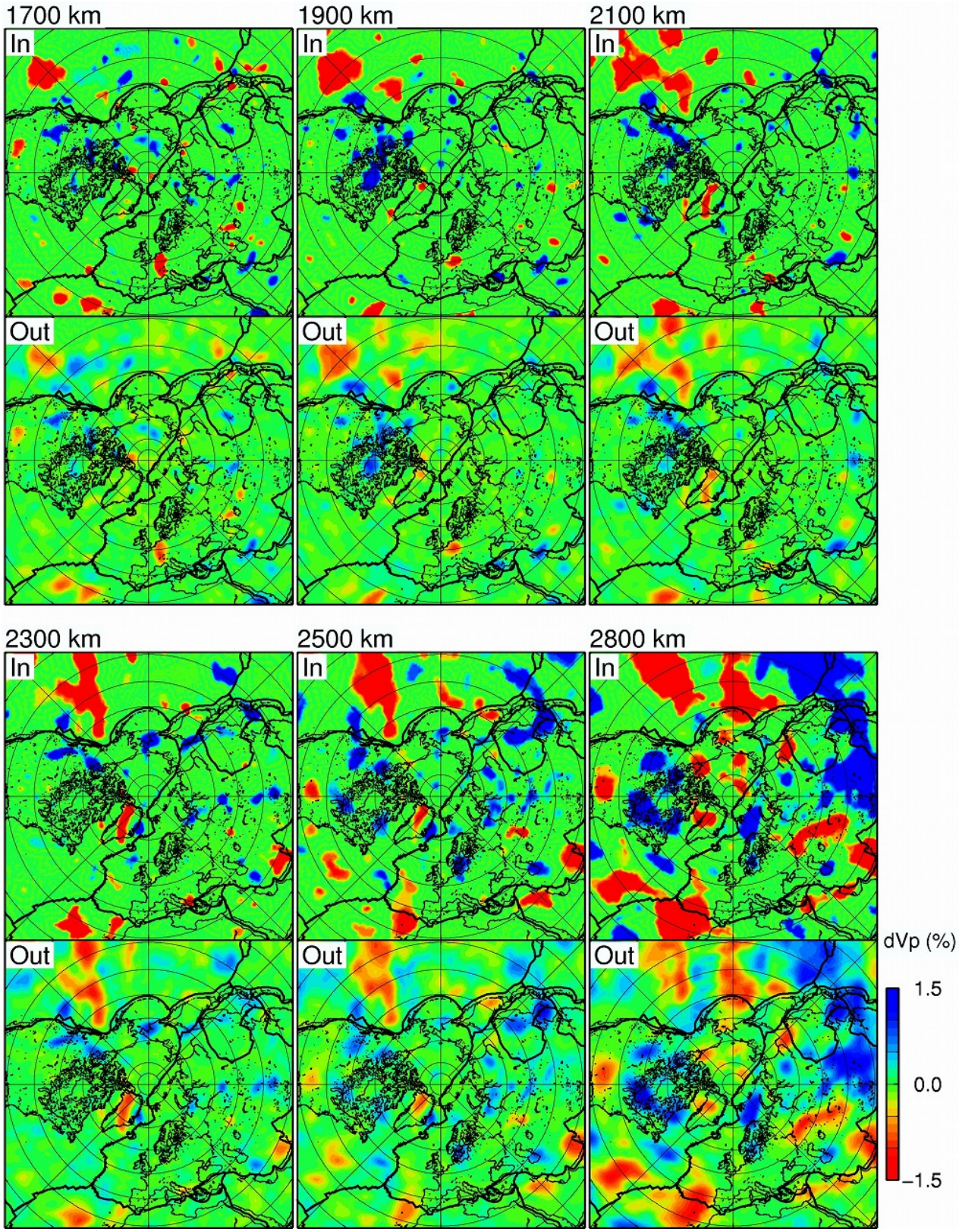

Figure S24. (continued)

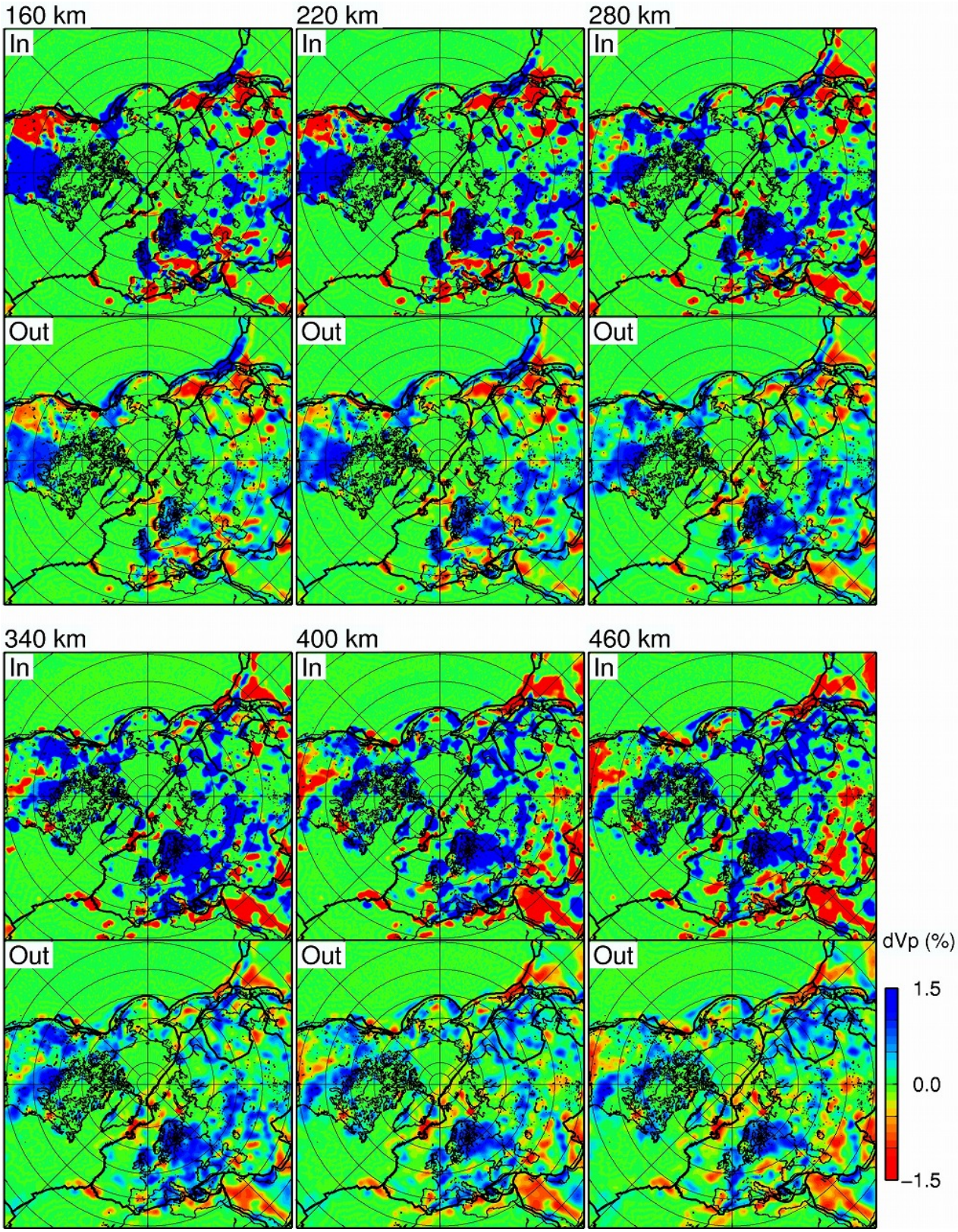
160 km
In
Out
220 km
In
Out
280 km
In
Out
340 km
In
Out
400 km
In
Out
460 km
In
Out
dVp (%)
1.5
0.0
−1.5

Figure S25.

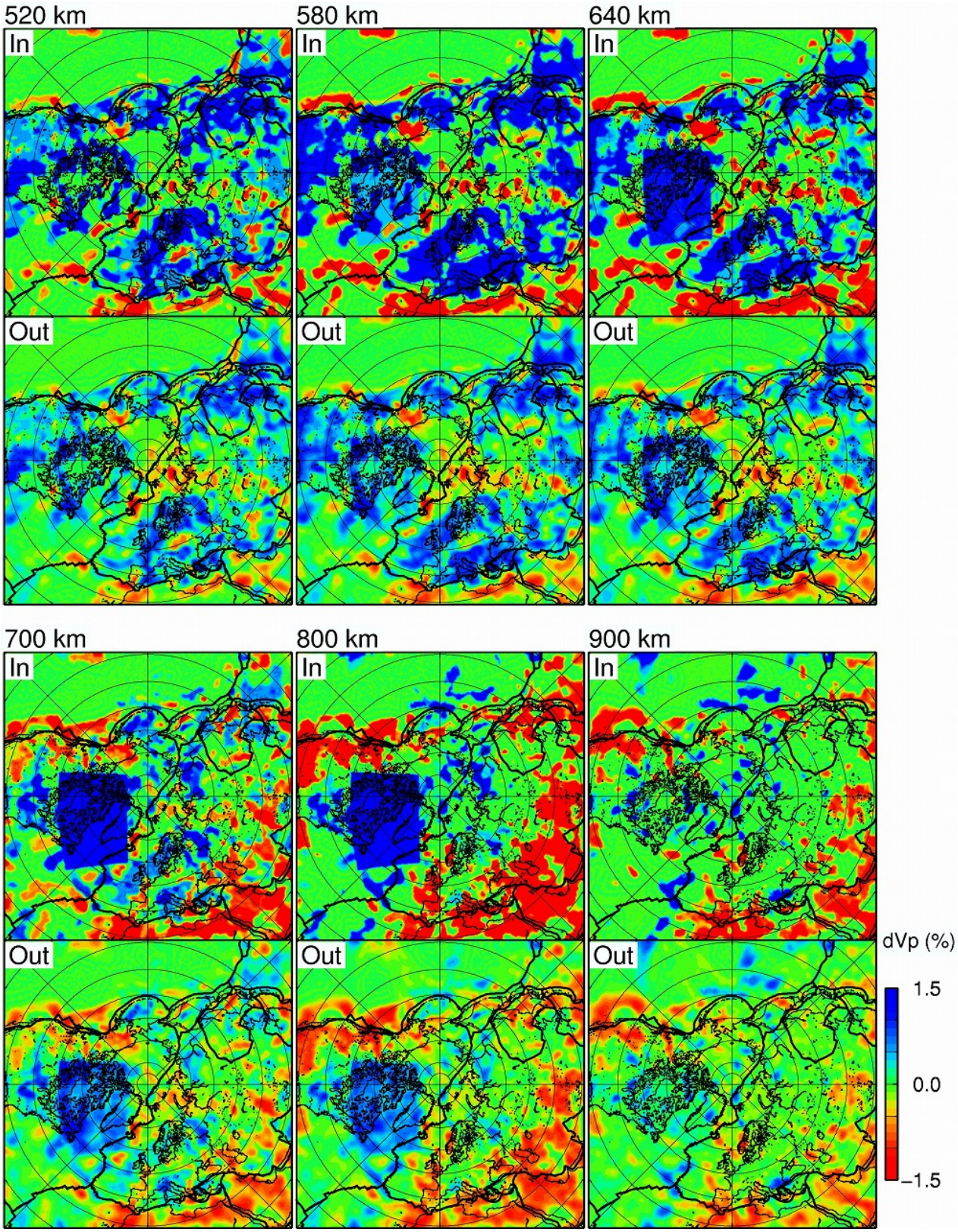

Figure S25. (continued)

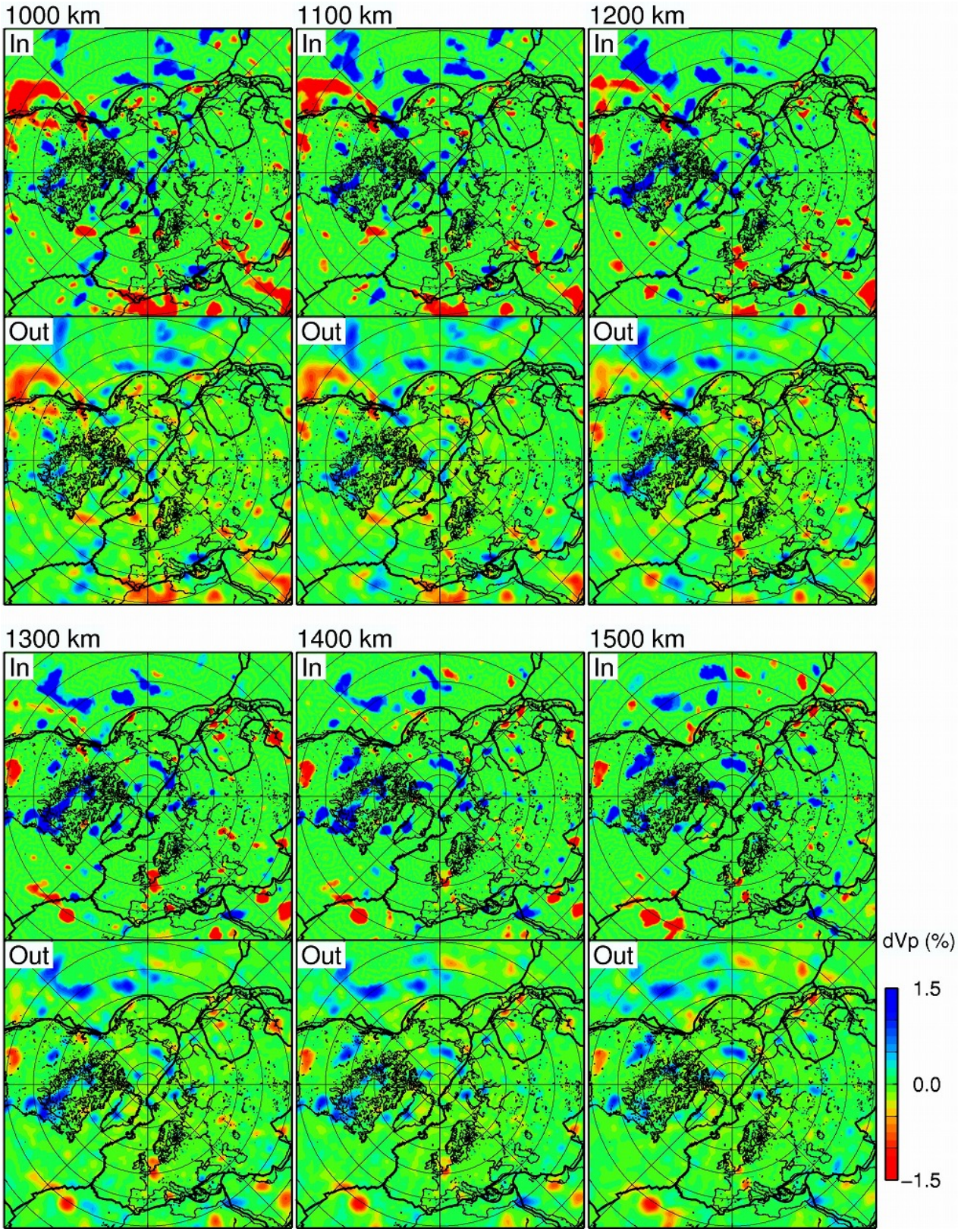

Figure S25. (continued)

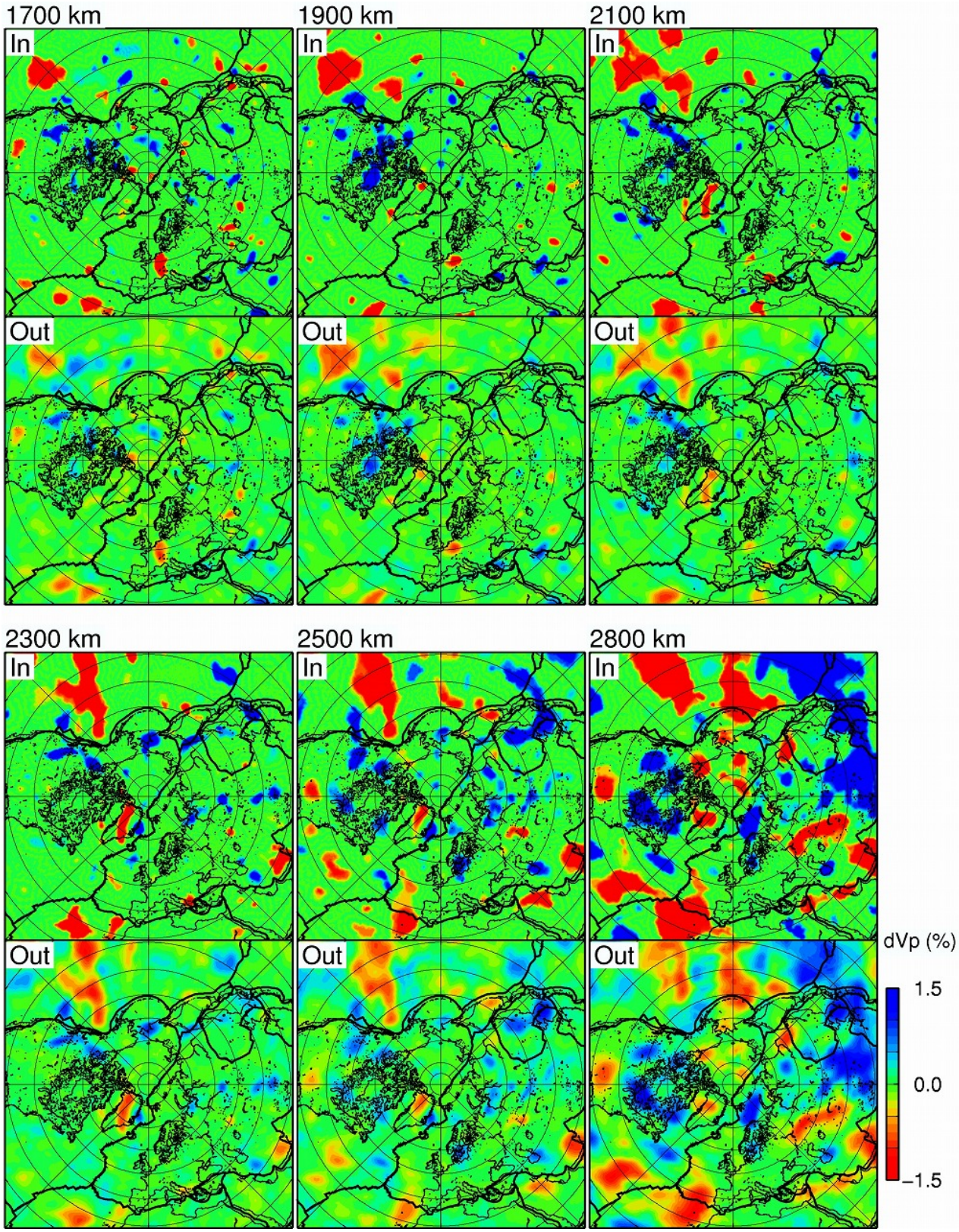

Figure S25. (continued)

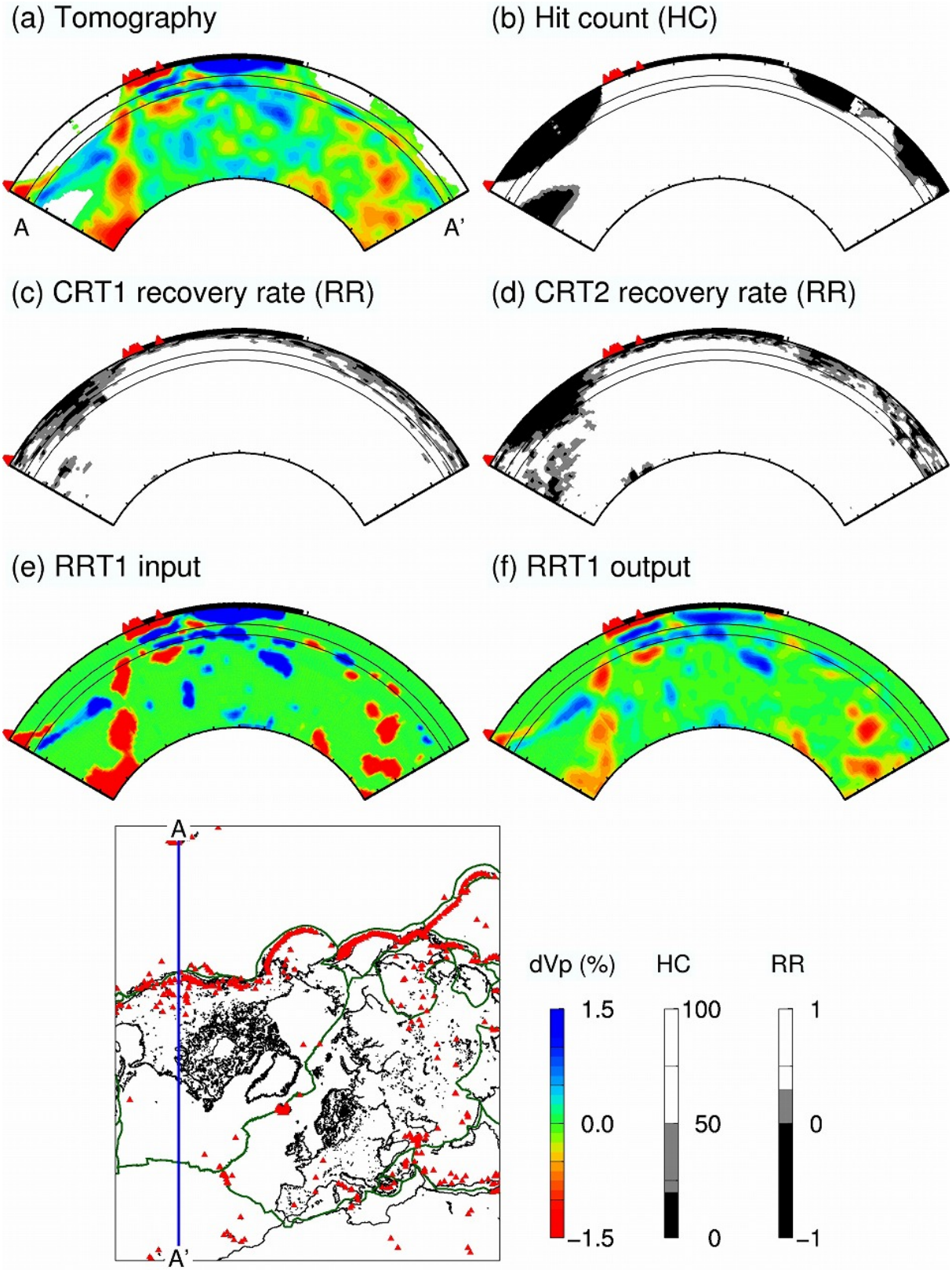
(a) Tomography
A
A'
(b) Hit count (HC)
(c) CRT1 recovery rate (RR)
(d) CRT2 recovery rate (RR)
(e) RRT1 input
(f) RRT1 output
A
A'
dVp (%)
1.5
0.0
−1.5
HC
100
50
0
RR
1
0
−1

Figure S26.

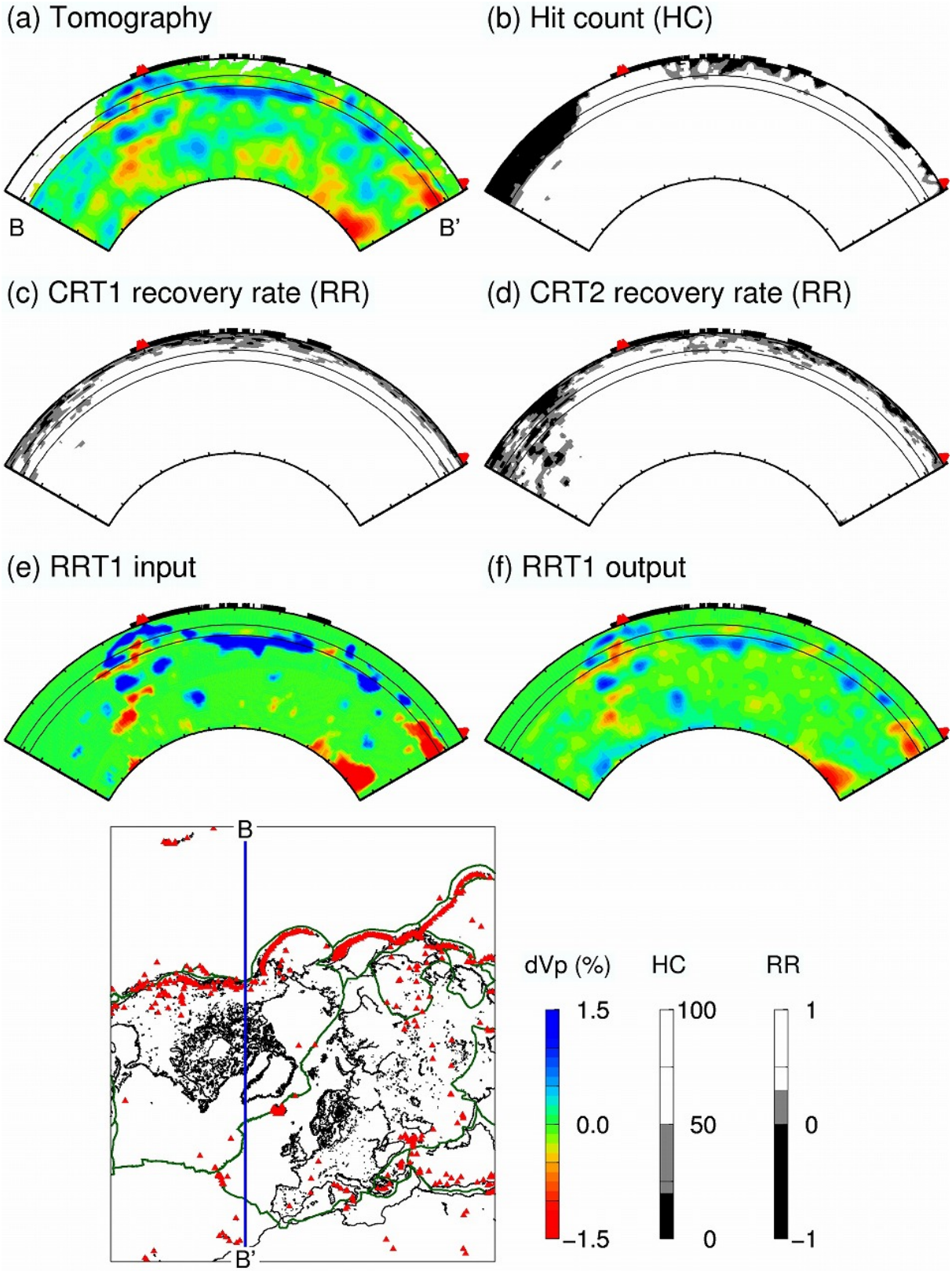
(a) Tomography
B
B'
(b) Hit count (HC)
(c) CRT1 recovery rate (RR)
(d) CRT2 recovery rate (RR)
(e) RRT1 input
(f) RRT1 output
B
B'
dVp (%)
1.5
0.0
−1.5
HC
100
50
0
RR
1
0
−1

Figure S27.

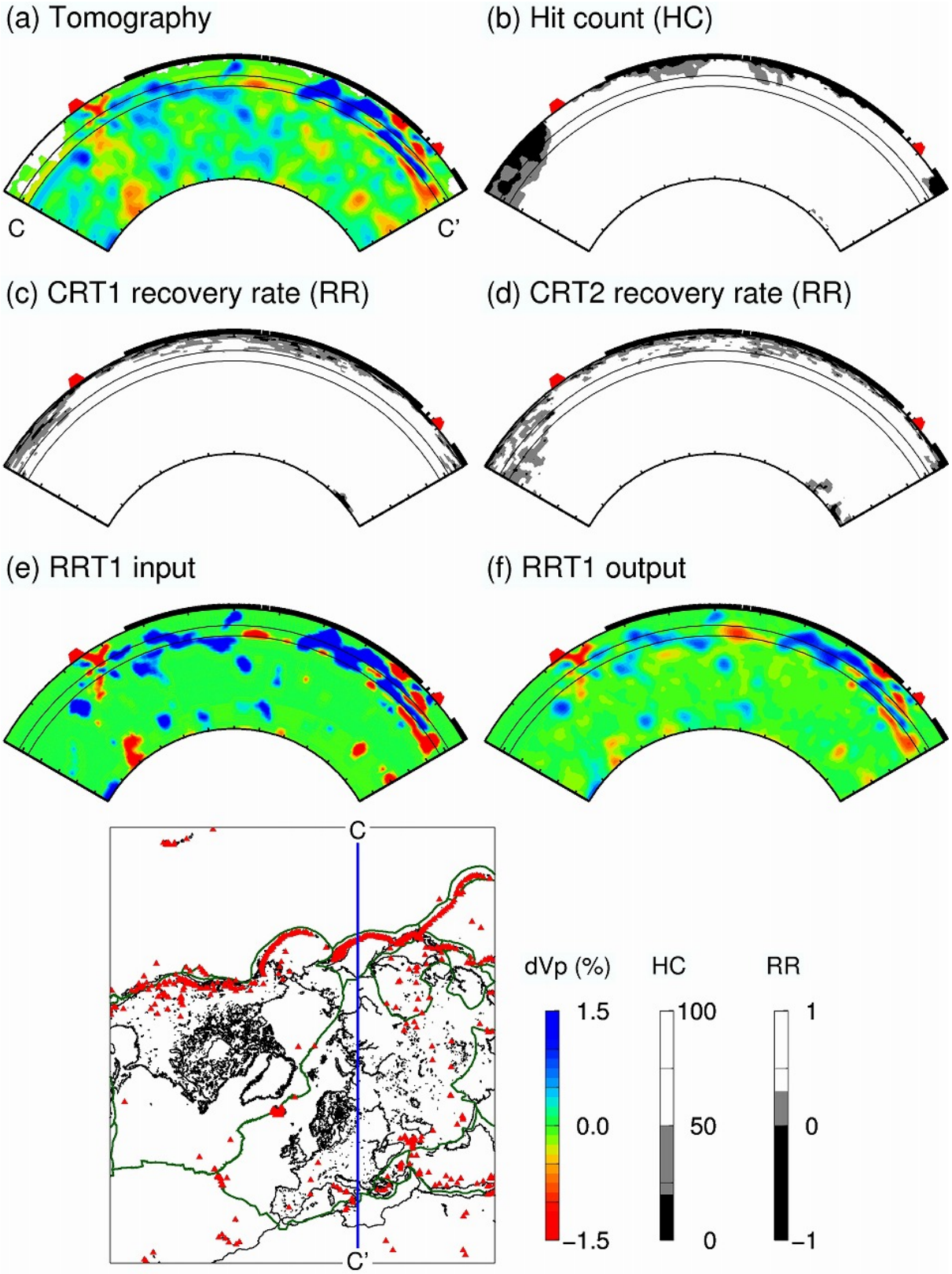
(a) Tomography
(b) Hit count (HC)
C
C'
(c) CRT1 recovery rate (RR)
(d) CRT2 recovery rate (RR)
(e) RRT1 input
(f) RRT1 output
C
C'
dVp (%)
1.5
0.0
−1.5
HC
100
50
0
RR
1
0
−1

Figure S28.

Figure S22. Map views of recovery rate (RR) estimated from the result of a checkerboard resolution test with a lateral grid interval of 278 km (a great circle distance of 2.5° on the surface) (CRT1). The layer depth is shown above each map. The RR scale is shown on the right. Red triangles: active volcanoes; thick black lines: plate boundaries.

Figure S23. The same as Figure S22 but estimated from the result of a checkerboard resolution test with a lateral grid interval of 167 km (a great circle distance of 1.5° on the surface) (CRT2).

Figure S24. Map views showing the input model (upper panels) and output results (lower panels) of RRT1. The layer depth is shown above each upper panel. The blue and red colors denote high and low Vp perturbations, respectively, whose scale (in %) is shown on the right. The thick black lines denote plate boundaries.

Figure S25. The same as Figure S24 but for RRT2.

Figure S26. Vertical cross sections along A-A' profile on the inset map showing **(a)** the obtained tomographic model, **(b)** average ray hit count (HC), **(c)** recovery rate (RR) from the CRT1, **(d)** RR from the CRT2, **(e)** input model of RRT1, and **(f)** output result of RRT1. The 410-km and 660-km discontinuities are shown in black solid lines. The thick black lines on the surface denote land areas. The red triangles denote active volcanoes. Red triangles: active volcanoes; thick green lines on the map: plate boundaries.

Figure S27. The same as Figure S26 but along B-B' profile on the inset map.

Figure S28. The same as Figure S26 but along C-C' profile on the inset map.

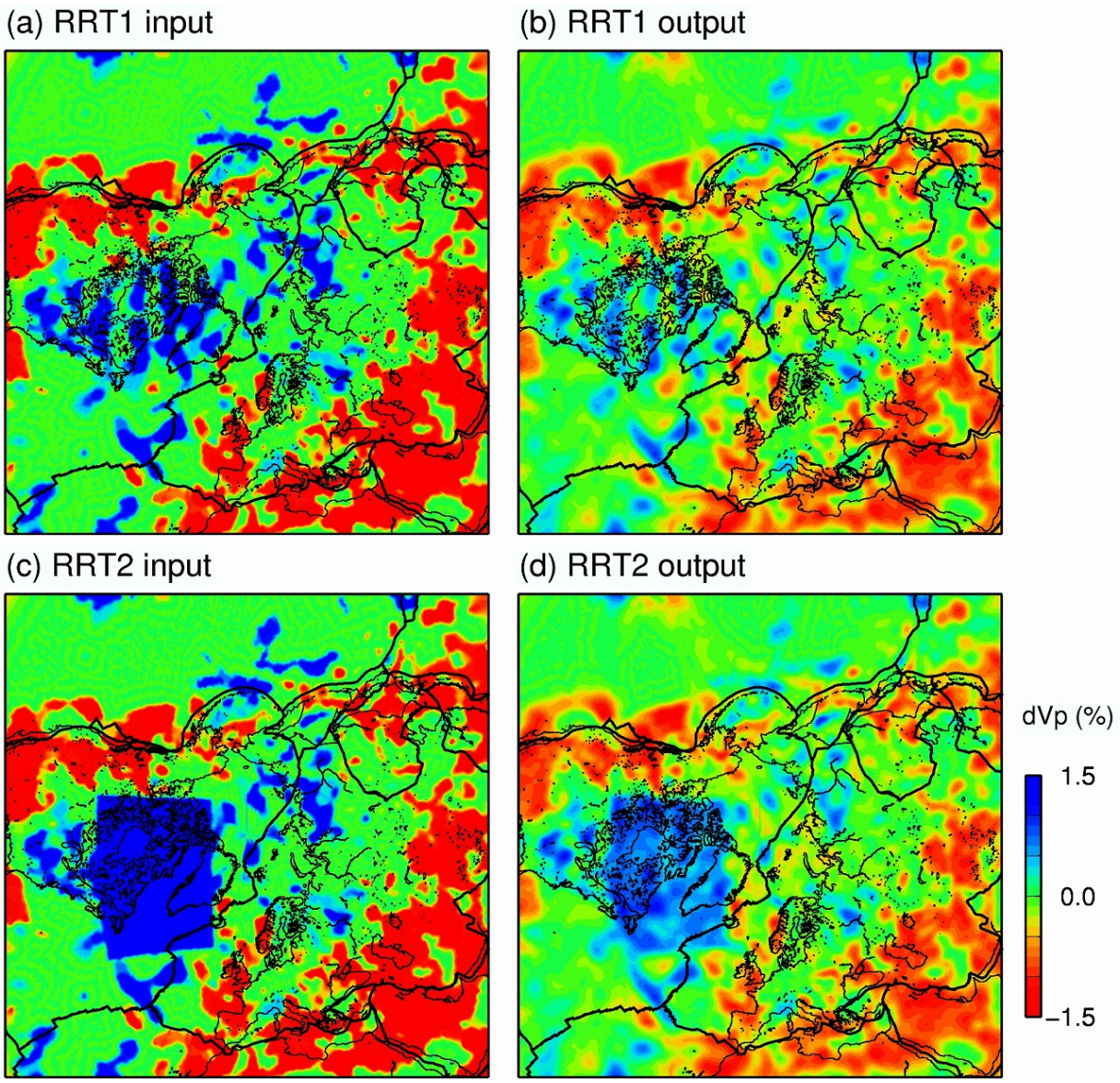

Figure S29. Comparison of the RRT results at a depth of 800 km. **(a)** The RR1 input model, **(b)** the RRT1 output result, **(c)** the RR2 input model, and **(d)** the RRT2 output result. The blue and red colors denote high and low Vp perturbations, respectively, whose scale (in %) is shown on the right. The thick black lines denote plate boundaries.

Table S1. Information on the eight resolution tests conducted by this study.

Region	Center (lon, lat)	Block size	$N_{station}$ (inside)	$N_{station}$ (total)	N_{event}	N_P	N_{pP}	N_{PP}	N_{total}
1	(0.0, 90.0)	0.1° x 5.0 km (in) 1.0° x 20.0 km (out)	923	12,543	17,827	5,762,140	188,989	128,476	6,079,605
2	(-38.461, 90.0)	0.1° x 5.0 km (in) 1.0° x 20.0 km (out)	1,295	12,640	19,045	6,084,018	196,719	130,135	6,410,872
3	(-100.0, 60.0)	0.1° x 5.0 km (in) 1.0° x 20.0 km (out)	4,164	12,612	17,671	5,738,009	190,145	129,393	6,057,547
4	(110.0, 50.0)	0.7° x 10.0 km (in) 1.3° x 20.0 km (out)	1,183	12,485	16,033	5,623,441	183,447	122,100	5,928,988
5	(80.0, 60.0)	0.2° x 10.0 km (in) 1.0° x 20.0 km (out)	1,028	12,555	19,288	6,006,788	197,460	131,146	6,335,394
6	(-70.0, 50.0)	0.1° x 5.0 km (in) 1.0° x 20.0 km (out)	2,469	12,565	17,167	5,658,950	178,360	127,522	5,964,832
7	(-120.0, 35.0)	0.1° x 5.0 km (in) 1.0° x 20.0 km (out)	3,618	12,612	19,817	6,190,973	206,735	134,798	6,532,506
8	(-170.0, 40.0)	0.3° x 10.0 km (in) 1.0° x 20.0 km (out)	705	12,659	19,515	6,448,371	209,746	134,384	6,792,501
9	(150.0, 35.0)	0.7° x 10.0 km (in) 1.3° x 20.0 km (out)	1,021	12,611	17,150	5,907,332	186,988	127,138	6,221,458
10	(60.0, 35.0)	0.3° x 10.0 km (in) 1.0° x 20.0 km (out)	2,307	12,551	19,120	5,974,579	198,425	131,238	6,304,242
11	(10.0, 40.0)	0.1° x 5.0 km (in) 1.0° x 20.0 km (out)	3,863	12,558	19,078	5,919,055	187,066	129,807	6,235,928
12	(-30.0, 35.0)	0.1° x 5.0 km (in) 1.0° x 20.0 km (out)	1,687	12,542	17,276	5,664,954	178,391	126,679	5,970,024

Table S2. Number of grid nodes at each depth which are arranged for conducting the tomographic inversion.

Grid depth (km) inside study region	Grid used outside study region	Number of nodes
15.0	o	23,453
32.5	-	13,955
50.0	o	23,325
75.0	-	13,744
100.0	o	22,917
140.0	-	13,491
180.0	o	22,270
220.0	-	13,095
260.0	o	21,811
300.0	-	12,817
340.0	o	21,191
380.0	-	12,438
420.0	o	20,686
460.0	-	12,169
500.0	o	20,039
575.0	-	11,723
650.0	o	19,027
725.0	-	11,114
800.0	o	18,005
875.0	-	10,519
950.0	o	17,185
1025.0	-	9,946
1100.0	o	16,257
1200.0	-	9,344
1300.0	o	15,027
1400.0	-	8,627
1500.0	o	13,837
1600.0	-	7,935
1700.0	o	12,703
1800.0	-	7,360
1900.0	o	11,738
2000.0	-	6,724
2100.0	o	10,693
2200.0	-	6,112
2300.0	o	9,695
2425.0	-	5,500
2550.0	o	8,523
2675.0	-	4,809
2800.0	o	7,551
Total		527,355

References

Amaru, M. L. (2007). Global travel time tomography with 3-D reference models. Doctoral thesis, Utrecht University. https://dspace.library.uu.nl/handle/1874/314949

Hosseini, K., Matthews, K. J., Sigloch, K., Shephard, G. E., Domeier, M., & Tsekhmistrenko, M. (2018), SubMachine: Web-Based tools for exploring seismic tomography and other models of Earth's deep interior. *Geochemistry, Geophysics, Geosystems*, 19(5), 1464-1483. https://doi.org/10.1029/2018GC007431

Kennett, B. L. N., & Engdahl, E. R. (1991). Traveltimes for global earthquake location and phase identification. *Geophysical Journal International*, 105, 429–465. https://doi.org/10.1111/j.1365-246X.1991.tb06724.x

Lu, C., Grand, S. P., Lai, H., & Garnero, E. J. (2019). TX2019slab: A new P and S tomography model incorporating subducting slabs. Journal of Geophysical Research: Solid Earth, 124, 11549–11567. https://doi.org/10.1029/2019JB017448

Ritsema, J., Deuss, A., van Heijst, H. J., & Woodhouse, J. H. (2011). S40RTS: a degree-40 shear-velocity model for the mantle from new Rayleigh wave dispersion, teleseismic traveltime and normal-mode splitting function measurements. Geophysical Journal International, 184, 1223–1236. https://doi.org/10.1111/j.1365-246X.2010.04884.x

Simmons, N. A., Forte, A. M., Boschi, V., & Grand, S. P. (2010). GyPSuM: A joint tomographic model of mantle density and seismic wave speeds. Journal of Geophysical Research: Solid Earth, 115(B12), B12310. https://doi.org/10.1029/2010JB007631

Simmons, N. A., Myers, S. C., Johannesson, G., & Matzel, E. (2012). LLNL-G3Dv3: Global P wave tomography model for improved regional and teleseismic travel time prediction. Journal of Geophysical Research: Solid Earth, 117, B10302. https://doi.org/10.1029/2012JB009525